Materials Science & Engineering A 971 (2026) 150362

Contents lists available at ScienceDirect

Materials Science & Engineering A

journal homepage: www.elsevier.com/locate/msea

Plastic deformation in nanotwinned copper mediated by source mechanisms based on Frank dislocations

D. Liu [a], D. Weygand [a,*], J. Li [a], C. Kirchlechner [a], P. Gumbsch [a,b]

[a] Institute for Applied Materials (IAM), Karlsruhe Institute of Technology (KIT), Kaiserstr. 12, Karlsruhe, 76131, Germany
[b] Fraunhofer Institut für Werkstoffmechanik (IWM), Wöhlerstr. 11, Freiburg, 79108, Germany

ARTICLE INFO

Keywords:
Frank dislocation at twin boundary
Nanotwins
Dislocation source mechanism
Molecular dynamics simulations

ABSTRACT

Frank partial dislocations are common defects at twin boundaries that can be found at annealing twins or formed by dislocation-twin boundary interactions. These sessile twin boundary dislocations favor dislocation emission from twin boundaries as reported in literature, to explain reduced pop-in stresses during nanoindentation in Cu near a twin boundary. This study presents molecular dynamics simulation results for Cu samples, containing a twin boundary with an initial Frank partial dislocation dipole. The postulated nucleation of a 60° lattice dislocation from dissociated Frank partial dislocations at twin boundary is confirmed and its energetics is discussed. Two cooperative transmission & reflection mechanisms triggered by the interaction of 60° lattice dislocations and twin boundaries are identified. For a single 60° lattice dislocation captured within a twin lamella a new stable dislocation source mechanism is uncovered, emitting screw dislocations to both sides of the lamella. The source relies on the cooperative transmission & reflection mechanisms, occurring on both twin boundaries forming the lamella. This new stable source mechanism could contribute to explain extended plastic deformation in nanotwinned materials.

1. Introduction

The strength of crystalline materials, including nanocrystalline metals, is determined by their resistance to dislocation motion. Traditional strengthening methods rely on the introduction of point defects, voids, particles, or grain refinement to create barriers to dislocation motion [1,2]. In nanocrystalline metals, the nanoscale grain size results in a high density of grain boundaries (GBs), which effectively blocks dislocation propagation. However, this comes with limited dislocation storage ability, leading to high strength but reduced ductility [3], resulting in the typical strength–ductility trade-off. Coherent twin boundaries (TBs) can effectively hinder dislocation motion similar to the GB strengthening mechanism, while also providing dislocation accumulation sites and slip channels permitting increased ductility [4–6]. Therefore, nanotwinned copper, which contains layered and coherently grown twin boundaries with nanosized spacing, exhibits the combination of ultrahigh yield strength and high ductility [7,8].

The continued plasticity due to dislocation glide in nanotwinned materials is controlled by the availability of dislocation sources, as the spacing for bulk like dislocation multiplication is too confined within a nanosized twin lamella [9]. GBs are considered to be the primary nucleation sites of dislocations [10,11], while TBs exhibit much lower excess energies and significantly greater mechanical stability [12]. As a result, perfect TBs are unlikely to act as potential dislocation sources. However, TBs in all types of processing routes whether deformation, growth, or annealing twins are inherently imperfect and should be regarded as defective entities [8,13,14]. It has been demonstrated that sessile TB steps enhance dislocation emission from TBs due to the significant stress concentration effect [5,6,15,16]. Lu et al. [17] revealed the dependence of the dislocation nucleation site, e.g. TB/GB junction or steps on TBs, on the twin lamella spacings. They concluded that the observed TB steps are sessile TB dislocations having a dissociated core and induce displacements perpendicular to the twin plane. These sessile TB dislocation configurations can be dissociated Frank partial dislocations at TBs [18], which are commonly observed as TB defects [7,19–23].

Lu et al. [17] emphasized that dislocation emission from TB dislocations can be considered as a dislocation dissociation process and its activation stress is only related to the Burgers vector of the TB dislocation and the emitted dislocation. Li et al. [24] provide indirect experimental evidence for a Frank partial dislocation at TB acting as a dislocation source in copper by analyzing the pop-in stresses measured during nanoindentation on a single crystal and a bi-crystal containing a twin boundary. They found that the stress required to activate a dislocation source on a TB in copper and its alloys is approximately

* Corresponding author.
E-mail address: daniel.weygand@kit.edu (D. Weygand).

https://doi.org/10.1016/j.msea.2026.150362
Received 9 December 2025; Received in revised form 30 April 2026; Accepted 4 May 2026
Available online 25 May 2026

80 % of the stress observed for copper bulk single crystals. To explain the ratio of activation stresses, they propose that pre-existing Frank partial dislocations at the TB split into two mobile dislocations: an emitted lattice dislocation and a residual mobile TB Shockley partial dislocation. The reported activation shear stress ratio is in agreement with the isotropic elastic energy estimates associated with the proposed dissociation mechanism of the Frank partial dislocation. They estimated that the activation shear stress is at least 1.6 GPa in case of twinned samples.

The dislocation emission from a TB dislocation is highly localized, occurs on very short timescales, and is driven by high stresses, making its direct experimental observation extremely challenging. In this study, molecular dynamics (MD) simulations enable atomic-scale tracking of dislocation nucleation, providing valuable insights into the proposed mechanism. Moreover, given the reported density of preexisting Frank partial dislocations on TBs, the dislocation density directly nucleated from the initial Frank partial dislocation may still be insufficient to fully account for the high ductility observed in nanotwinned metals. This raises the question of whether twin lamellae can be involved in regeneration of dislocation sources in nanotwinned structures. Therefore, the interaction of lattice dislocations originating from the dissociation of Frank partial dislocations and twin boundaries is systematically studied here.

2. Method

Atomistic simulations for copper are performed using the LAMMPS software package [25] to investigate the behavior of Frank partial dislocations on a twin boundary with and without applied loading. The Embedded Atom Method (EAM) potential of Mishin et al. [26] for Cu is used. Atomsk [27] is employed to generate the twinned samples and to introduce the Frank partial dislocations on the TB, based on elastic displacement fields [28]. The atomic structures and dislocations are identified and visualized using the software OVITO [29]. Common Neighbor Analysis (CNA) is applied to color the atoms: blue for face-centered cubic (FCC) structures, red for hexagonal close-packed (HCP) structures, and white for other configurations. The dislocation analysis is performed using the OVITOs' Dislocation Extraction Algorithm (DXA) [30]. Here, the right-hand finish–start (FS/RH) convention for Burgers vectors is used.

2.1. Structure: Frank partial dislocations at a TB

Twinned samples are generated with a twin spacing of $\lambda \approx 40\,\mathrm{nm}$ (Fig. 1(a)) to investigate the relaxed structure of Frank partial dislocations on a TB. The edges of the cuboid simulation cell (X, Y, Z) and the crystal orientations of the matrix, marked by M, are aligned as follows: $X \parallel [111]$, $Y \parallel [10\bar{1}]$, $Z \parallel [\bar{1}2\bar{1}]$. The positions of the atoms on the matrix side are mirrored with respect to the twin plane (111) to obtain the twin side (T). The samples sizes L_x, L_y, L_z are $\approx 80.15\,\mathrm{nm},\ 2.04\,\mathrm{nm}$ and $80.15\,\mathrm{nm}$. The sample comprises about one million atoms. A Frank partial dislocation dipole with the dipole distance $d = 1/2L_z \approx 40\,\mathrm{nm}$ is introduced on the TB. The dislocation dipole is modeled as infinitely long in Y direction and is fully compatible with periodic boundary conditions applied in all spacial directions.

Following the naming convention of Marquis and Medlin [18], the two distinct Frank partial dislocations in the dipole (Fig. 1(b)) are referred to as the exterior and interior Frank partial dislocations. This classification considers both the location of the extra atomic layer linked to each Frank partial dislocation and whether the angle between the TB and the inclined glide planes $\{111\}$ is acute or obtuse:

- exterior Frank partial dislocation: extra atomic layer on the obtuse side
- interior Frank partial dislocation: extra atomic layer on the acute side

Fig. 1(b) shows the atomic (core) structures of the exterior and interior Frank partial dislocations at the TB prior to relaxation. The initial TB plane is a B layer in the stacking sequence A|B|ACBA. In the middle of the sample, an atomic layer A on the right side of the TB plane is effectively removed, causing the TB plane to shift from position B to C in the stacking sequence AB|C|BA. The direction of the extra atomic half-layer follows the $\vec{t}\times\vec{b}$ rule, where the dislocation line direction $\vec{t}$ is parallel to the $+Y$ direction and the Burgers vector $\vec{b}$ points in the $-X$ or $+X$ direction.

Fig. 1(c) presents the annotated double Thompson tetrahedron alongside the relevant slip planes for the sample. The TB plane is highlighted as the common ABC (111) plane. The mirror-symmetrical slip planes BCD in the matrix (M) and $C^TB^TD^T$ in the twin (T) are illustrated, together with their associated Burgers vectors of matrix and twin dislocations.

2.2. Relaxation scheme and energy barrier calculation

To obtain relaxed structures of the Frank partial dislocations at the TB, the potential energy is in a first step minimized using the conjugate gradient method to achieve a stress-free simulation box size. This is followed by energy minimization at 0 K employing the fast inertial relaxation algorithm (FIRE) [31]. An annealing relaxation is performed after the initial energy minimization to ensure reaching fully relaxed configurations. The annealing relaxation scheme comprises three steps: first, the sample is relaxed at 0.1 K. Next, it is gradually heated to 300 K and maintained at this temperature for equilibration. Finally, it is cooled back down to 0.1 K and equilibrated to complete relaxation. The heating and cooling processes are carried out using the Nosé–Hoover thermostat and barostat (NPT ensemble), allowing the simulation cell to expand or shrink with a temperature change rate of $1.5\,\mathrm{K\,ps^{-1}}$. During the constant temperature holds, at 0.1 K and 300 K, the system is first equilibrated under stress-free conditions using the NPT ensemble for 60 ps, followed by an NVT ensemble hold for another 60 ps. A time step of 1 fs is employed. After completion of the annealing relaxation, the potential energy is again minimized using the FIRE algorithm.

To evaluate energy barriers associated with the dissociation of Frank partial dislocations at the twin boundary, the climbing-image nudged elastic band (CI-NEB) method is employed [25]. The reaction pathway is constructed to map the minimum energy path (MEP) using 30 replicas and a NEB spring constant of $0.1\,\mathrm{eV\AA^{-2}}$. The potential energy along the MEP is minimized using the quickmin algorithm with a force convergence criterion of $0.005\,\mathrm{eV\,\AA^{-1}}$. A time step of 10 fs is employed.

2.3. Twin boundary dislocation: elastic strain energy and core energy

For the following energetic analysis, we assume the sample size, the Frank partial dislocation dipole spacing d, and the twin lamella spacing λ large enough to neglect the influence of periodic boundary conditions. Interactions between periodic images of dislocation dipoles or quadruples are known to be significant at small sample sizes [32–34]. The system size in this study is chosen large enough so that the stacking fault width d_{SF}, used as sensitivity indicator, is unaffected (see Appendix A). In the following analysis, the Frank partial dislocations are treated as quasi-independent dislocations to investigate their relaxed core structures and energies.

The total energy E_{tot} associated with each type of Frank partial dislocation is evaluated within a cylindrical region of radius R (where $R < \lambda$ and $R < d/2$) centered along the dislocation line at the twin boundary. The total energy E_{tot}, defined as the sum of the potential energy of all atoms within the cylindrical region, can be expressed as the sum of the following energy contributions [28,35],

$$E_{\mathrm{tot}}(R) = E_{\mathrm{disloc}}(R)L + N(R)E_{\mathrm{coh}} + E_{\mathrm{TB}}(R, \gamma_{\mathrm{TB}}) \tag{1}$$

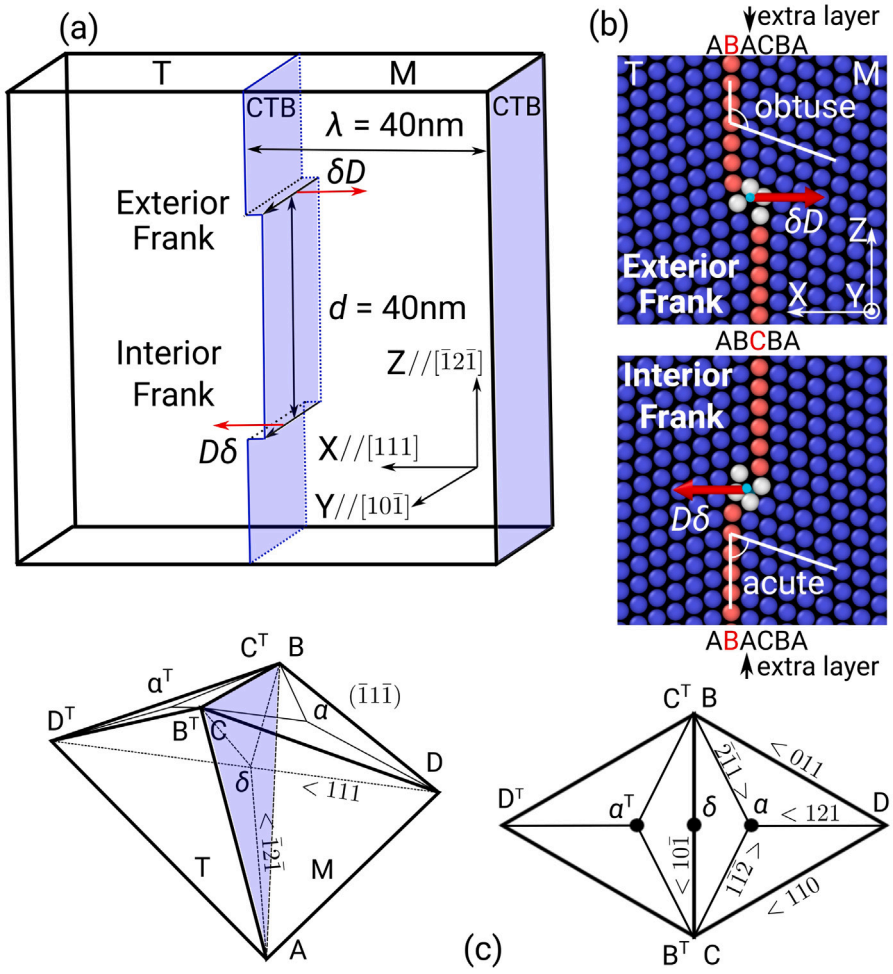

Fig. 1. The initial unrelaxed Frank dislocation dipole at a TB in a twinned bicrystal. (a) Frank dislocation dipole at TB having a separation distance $d \approx 40\,\text{nm}$ and twin spacing $\lambda \approx 40\,\text{nm}$ (b) Detailed view of the exterior and interior Frank dislocations showing the extra atomic layer on the obtuse side and on the acute side. Burgers vectors are scaled by a factor 4. The dislocation line direction BC is along the $+Y$ axis. (c) Left: Double Thompson tetrahedron with the ABC (111) TB plane. Right: top view on the unfolded BCD glide planes on matrix and twin sides including the notation for the partial dislocations used during analysis.

where $E_{\text{disloc}}(R)$ denotes the dislocation energy per unit length for an infinite straight dislocation within the cylindrical region. The dislocation length is L, and $N(R)$ represents the number of atoms contained within the cylindrical region. For copper, the cohesive energy per atom is $E_{\text{coh}} = -3.54\,\text{eV}$ [26]. The twin boundary energy within the cylindrical region is $E_{\text{TB}} = 2RL\gamma_{\text{TB}}$, where γ_{TB} is the TB energy per unit area.

The dislocation energy per unit length $E_{\text{disloc}}(R)$ consists of the elastic strain energy $E_{\text{el}}(R, r_c)$ and the dislocation core energy $E_{\text{c}}(r_c)$:

$$E_{\text{disloc}}(R) = E_{\text{el}}(R, r_{\text{c}}) + E_{\text{c}}(r_{\text{c}}) = E_{\text{pre}} \ln \frac{R}{r_c} + E_{\text{c}}(r_{\text{c}}) \tag{2}$$

where E_{pre} is the elastic energy pre-factor and r_{c} is the inner cut-off radius. Further details on the employed isotropic and anisotropic elastic energy pre-factors are provided in Appendix B.

The challenge of extracting E_{disloc} from E_{tot} lies in accurately estimating the twin boundary energy E_{TB}. The ideal TB energy $\gamma_{\text{TB}}^{\text{ideal}}$ is about half of the intrinsic stacking fault energy for Cu [36] and is reported to be strain dependent even for small deformations [37,38]. In our setup, the introduction of the Frank partial dislocation dipole is achieved by removing one {111} atomic layer between the Frank dislocation dipole from a total 384 atomic layers along the X direction, as illustrated in Fig. 1. Therefore, the periodic boundary conditions applied to the simulation cell (Fig. C.9(a)) will lead to constraints on the dislocations and TBs in X direction. Thus, the contribution of the TB energy E_{TB} cannot be directly evaluated using the unstrained TB energy $\gamma_{\text{TB}}^{\text{ideal}} = 22.22\,\text{mJ m}^{-2}$ [26]. The scheme used to estimate the TB energy is described in Appendix D. The resulting γ_{TB} values of the exterior and interior Frank partial dislocation of $\gamma_{\text{TB}}^{\text{ext}} \approx 1.159\gamma_{\text{TB}}^{\text{ideal}}$ and $\gamma_{\text{TB}}^{\text{int}} \approx 1.144\gamma_{\text{TB}}^{\text{ideal}}$ are used for Eq. (1).

Once the twin boundary energy contribution $E_{\text{TB}}(R, \gamma_{\text{TB}})$ is known in Eq. (1), the dislocation energy $E_{\text{disloc}}(R)$ is accessible. For large $R \gg b$, the $E_{\text{el}}(R)$ scales linearly with $\ln(R/r_c)$, with the slope given by the energy prefactor E_{pre} (Eq. (2)). The dislocation core energy E_{c}, which accounts for all non-linear contributions, is obtained by extrapolating $E_{\text{disloc}}(R)$ from the elastic regime back to the chosen cutoff radius $r_{\text{c}} = b = 2.087\,\text{Å}$: From the slope E_{pre} of the graphs for both types (as shown later in Fig. 3(h)), the elasticity coefficients $K^{\text{ext}} = 79.19\,\text{GPa}$ resp. $K^{\text{int}} = 79.71\,\text{GPa}$ as well as the corresponding core energies $E_c^{\text{int,ext}}(r_c = b)$ are obtained using $K^{\text{int,ext}} = 4\pi E_{\text{pre}}^{\text{int,ext}}/b^2$. The core energies of the exterior and interior Frank partial dislocations are $E_{\text{c}}^{\text{ext}} = 0.226\,\text{eV nm}^{-1}$ and $E_{\text{c}}^{\text{int}} = 1.927\,\text{eV nm}^{-1}$. In Appendix C, results for a quadruple Frank partial dislocation configuration (Fig. C.9(b)), which minimizes the mechanical constraints of the dipole configuration, are summarized.

2.4. Frank partial dislocations on TBs under simple shear load

To investigate the dissociation reactions for the exterior and interior Frank partial dislocations under applied load, the nanotwinned samples

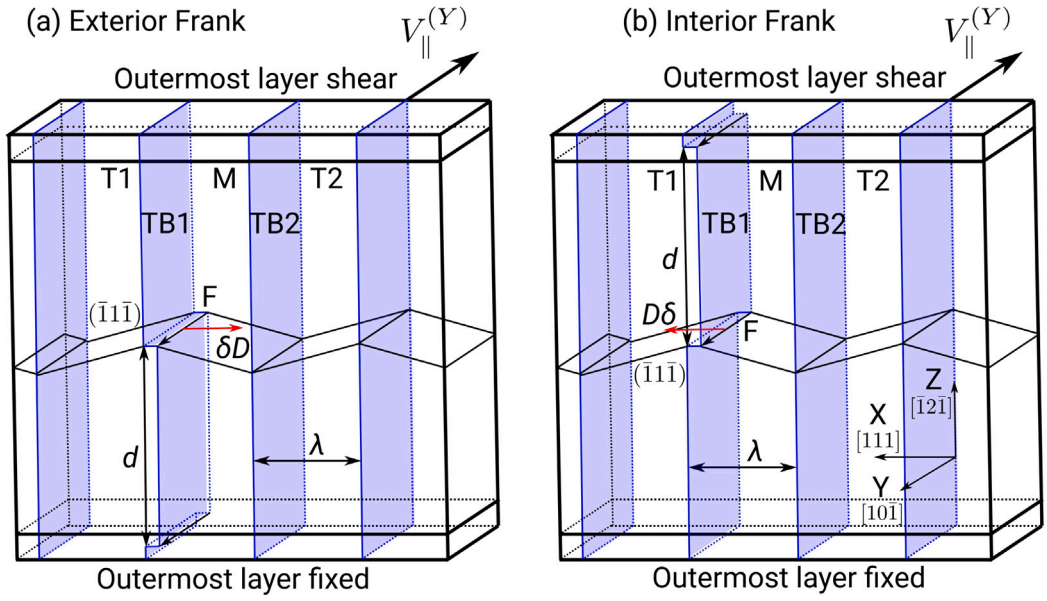

Fig. 2. Configuration of a nanotwinned sample with twin space $\lambda \approx 20\,\text{nm}$ containing a Frank partial dislocation dipole with separation distance $d \approx 40\,\text{nm}$ on TB1 with (a) exterior Frank dislocation δD (b) interior Frank dislocation $D\delta$ in the middle of sample. The respective counter part of each dipole is located in the top or bottom region used to control loading. The Frank partial dislocation dissociation and the dislocation-TB interactions are driven by a simple shear strain γ_{zy} antiparallel to dislocation line by relative movement between the top and bottom layers.

shown in Fig. 2 are used. The crystal orientations of the matrix and twin regions, as well as the simulation box dimensions are identical to those of the sample in Fig. 1(a). Both samples in Fig. 2 contain four TBs with a uniform twin spacing of $\lambda \approx 20\,\text{nm}$, which lies well within the convergence range of the stacking fault splitting width (Appendix A) while maintaining the same overall sample size and is consistent with previous studies on dislocation TB-interactions [39–41]. Furthermore, the dislocation energy shown in Fig. 3(h) demonstrates that, for distances larger than $R \approx 25b$ (corresponding to $\approx 5\ nm$), the energy follows the expected long-range behavior given by anisotropic elasticity, which is well below the chosen twin spacing. A Frank partial dislocation dipole, with line direction $\vec{t}$ parallel to Y axis and a separation distance $d \approx 40\,\text{nm}$ is introduced on TB1. In Fig. 2(a), the exterior type δD is placed in the center of the sample, while in Fig. 2(b) the interior type $D\delta$ is placed there, both are marked by the letter F. The associated Burgers vectors are indicated by red arrows. The respective dipole counterpart is placed in the outermost layers of the simulation box, which later serve as the region for applying strain controlled simple shear deformation. Periodic boundary conditions are applied in all directions during energy minimization and annealing relaxation. During mechanical loading, however, the periodic boundary condition in the Z direction is removed to enable the application of simple shear boundary conditions, while periodicity is preserved in the X and Y directions.

The eight outermost layers in the Z direction (i.e. the top and bottom regions of the sample) are constrained to undergo rigid body motion. A constant velocity of $10\,\text{m}\,\text{s}^{-1}$ along the $-Y$ direction is applied to the upper layer, while the lower layer remains fixed. Thus, the Frank partial dislocation in the middle of sample is activated by the applied shear strain, while the second Frank partial dislocation, located in the rigid control region, remains stationary. The relative motion between the upper and lower layers results in a constant engineering shear strain rate $\dot{\gamma}_{zy} \approx 1.3 \times 10^8\,\text{s}^{-1}$. To minimize the generation of elastic shock waves, a linearly varying velocity profile is initially assigned to the atoms between the control regions. These atoms between the bottom and top layers are allowed to evolve under a canonical ensemble (NVT) with a temperature maintained at 0.1 K, thereby suppressing thermal activation effects during the loading.

The applied simple shear generates symmetric shear stresses on the inclined $\{111\}$ BCD and $B^TC^TD^T$ glide planes in the matrix and the twin sides, while introducing no shear stress components on the twin boundary plane. In contrast, previous studies investigating the interactions between screw or 60° lattice dislocations with TBs have considered effective shear stresses acting directly on the twin plane in [39,40]. Additionally, in those studies, one of the inclined $\{111\}$ glide planes is oriented parallel to the sample surface leading to non-symmetric shear stresses on the slip planes of the matrix and twin side.

3. Result

We first analyze the relaxed atomic structures of the two types of Frank partial dislocations at the TB, along with their associated dislocation energies. Subsequently, we investigate the dissociation reactions of Frank partial dislocations leading to lattice dislocation emission and examine their further interactions with TB under applied simple shear loading in the nanotwinned sample.

3.1. Relaxed frank partial dislocations at TB

Figs. 3 (a–b) show the relaxed atomic structures for the exterior and interior Frank partial dislocations on the TB. The exterior Frank partial dislocation δD dissociates into a stair-rod dislocation $\delta\alpha$ at the TB and an emitted 90° Shockley partial dislocation αD connected by an intrinsic stacking fault of width $d_{SF} \approx 2.3\,\text{nm}$. The dissociation reaction is given by Eq. (3):

$$\begin{aligned} &\textbf{Exterior Frank } \delta D \rightarrow \quad \textbf{stair-rod } \delta\alpha + \quad \textbf{Shockley } \alpha D \\ &\qquad \tfrac{1}{3}[\bar{1}\bar{1}\bar{1}] \rightarrow \quad \tfrac{1}{6}[\bar{1}0\bar{1}] \quad + \quad \tfrac{1}{6}[\bar{1}2\bar{1}] \end{aligned} \tag{3}$$

The interior Frank partial dislocation $D\delta$ remains compact during relaxation.

At 300 K, the stacking fault for the exterior Frank partial dislocation extends to a width of $d_{SF} \approx 3.3\,\text{nm}$ (Fig. 3(c)). For the interior Frank partial dislocation, the initially compact core tends to dissociate into a TB Shockley partial dislocation $B\delta$ and two lattice Shockley partial dislocations $D\alpha$ and αB, resulting in the formation of a stacking fault with

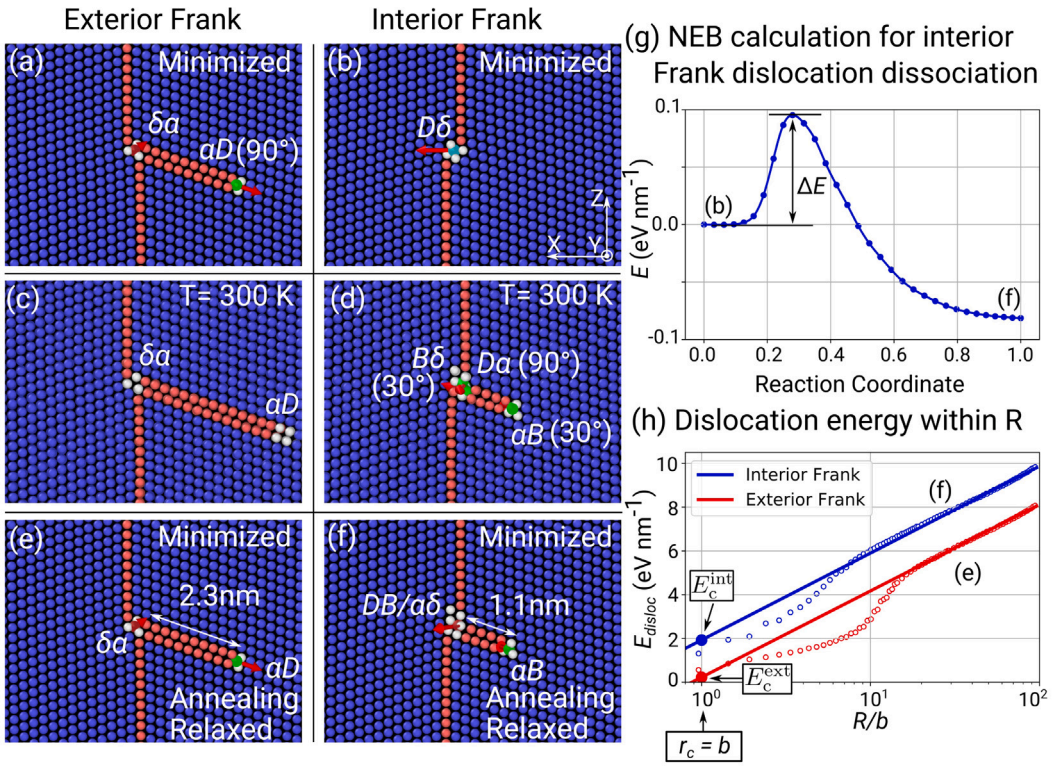

Fig. 3. Configuration of exterior and interior Frank partial dislocations before and after annealing relaxation on the left (a,c,d) resp. right column (b,d,f). The Burgers vectors are referring Thompson's notation in Figs. 1 (c–d). (a) The dissociated exterior Frank partial dislocation core with TB stair-rod dislocation $\delta\alpha$ ($\frac{1}{6}[\bar{1}0\bar{1}]$) before annealing relaxation. (b) The compact interior Frank partial dislocation cores before annealing relaxation. (c) The extending stacking fault width at 300 K. (d) The dissociated interior Frank partial dislocation with TB Shockley dislocation $B\delta$ ($\frac{1}{6}[2\bar{1}\bar{1}]$) at 300 K. (e) The restored exterior Frank partial dislocation core after annealing relaxation. (f) The dissociated interior Frank partial dislocation core with TB stair-rod dislocation $DB/\alpha\delta$ ($\frac{1}{6}$[310]) and an emitted αB Shockley partial dislocation after annealing relaxation. (g) CI-NEB calculation of the energy barrier ΔE of the dissociation reaction of the interior Frank partial dislocation (Eq. (4a)). (h) The dislocation energy $E_{\mathrm{disloc}}(R)$ dependency on $\ln(R/b)$. The dislocation core energy E_c^{int} and E_c^{ext} is obtained by extrapolating the elastic energy back to the core radius $r_c = b$.

a width of $d_{\mathrm{SF}} \approx 1.1$ nm shown in Fig. 3(d). After annealing relaxation and energy minimization the structure and stacking fault width for the exterior Frank partial dislocation return to their minimized state (Fig. 3(e)), while the interior Frank partial dislocation remains split (Fig. 3(f)) into a stair-rod dislocation $DB/\alpha\delta$ on the TB and an emitted 30° Shockley partial αB. The dissociation reaction is given by Eq. (4a) with the geometrically equivalent reaction in Eq. (4b). Both dissociation reactions can be observed during relaxation without applied stress.

$$\begin{aligned} &\textbf{Interior Frank } D\delta \rightarrow && \textbf{stair-rod } DB/\alpha\delta + && \textbf{Shockley } \alpha B \\ &\tfrac{1}{3}[111] \rightarrow && \tfrac{1}{6}[310] + && \tfrac{1}{6}[\bar{1}12] \end{aligned} \tag{4a}$$

$$\begin{aligned} &\textbf{Interior Frank } D\delta \rightarrow && \textbf{stair-rod } DC/\alpha\delta + && \textbf{Shockley } \alpha C \\ &\tfrac{1}{3}[111] \rightarrow && \tfrac{1}{6}[013] + && \tfrac{1}{6}[21\bar{1}] \end{aligned} \tag{4b}$$

The dissociation of the exterior Frank partial dislocation is a spontaneous reaction (Eq. (3)) without an energy barrier, while the dissociation of the interior Frank partial dislocation is only observed after application of the annealing relaxation scheme. To quantify the different dissociation behavior, the activation barrier for the dissociation reaction of the interior Frank partial dislocation during the annealing relaxation processes is calculated. Fig. 3(g) presents the results of the CI-NEB calculation, showing the total energy variation of the atoms surrounding the dislocation core within a cylindrical region of radius 20 nm plotted against the reaction coordinate for the dissociation of the interior Frank partial dislocation. The total energy of the initial compact core configuration (Fig. 3(b)) is taken as reference energy. The final, dissociated configuration (Fig. 3(f)) exhibits a lower total energy, indicating that the dissociation is energetically favorable. The difference in the saddle point energy and the reference energy gives the dissociation energy barrier $\Delta E \approx 0.095\,\mathrm{eV\,nm^{-1}}$. Fig. 3(h) shows the dislocation energy $E_{\mathrm{disloc}}(R)$ and is detailed in the methods section.

3.2. Frank partial dislocation dissociation under simple shear load

The configurations of individual Frank partial dislocation at TB are obtained using the annealing relaxation scheme on the structure shown in Fig. 2 with $\lambda \approx 20$ nm and $d \approx 40$ nm. Simple shear γ_{zy} is applied antiparallel to the direction of the dislocation line $\vec{t}$. Under applied load, both relaxed Frank partial dislocation types (Figs. 3 (e–f)) undergo further dissociation. This results in the emission of lattice dislocations, as displayed in Fig. 4.

For the exterior Frank partial dislocation shown in Fig. 4(a), once the shear stress reaches $\tau_{zy} \approx 2.22$ GPa corresponding to $\gamma_{zy} \approx 4.8\,\%$, the stair-rod dislocation $\delta\alpha$ on TB1 dissociates (Eq. (5)) into a mobile TB Shockley partial dislocation δC and a 30° trailing Shockley partial dislocation $C\alpha$ connected by a stacking fault of width ≈ 12.9 nm to the leading partial αD. The activation shear stress decreases to $\tau_{zy} \approx 1.8$ GPa at 300 K.

$$\begin{aligned} &\textbf{Stair-rod } \delta\alpha \rightarrow && \textbf{TB Shockley } \delta C + && \textbf{Trailing Shockley } C\alpha \\ &\tfrac{1}{6}[\bar{1}0\bar{1}] \rightarrow && \tfrac{1}{6}[11\bar{2}] + && \tfrac{1}{6}[\bar{2}\bar{1}1] \end{aligned} \tag{5}$$

For the interior Frank partial dislocation in Fig. 4(b), the dissociation of the TB stair-rod $DB/\alpha\delta$ dislocation occurs at a shear stress of $\tau_{zy} \approx 0.36$ GPa corresponding to $\gamma_{zy} \approx 0.78\,\%$ following Eq. (6): The dissociation products are a mobile TB Shockley partial dislocation $B\delta$ and

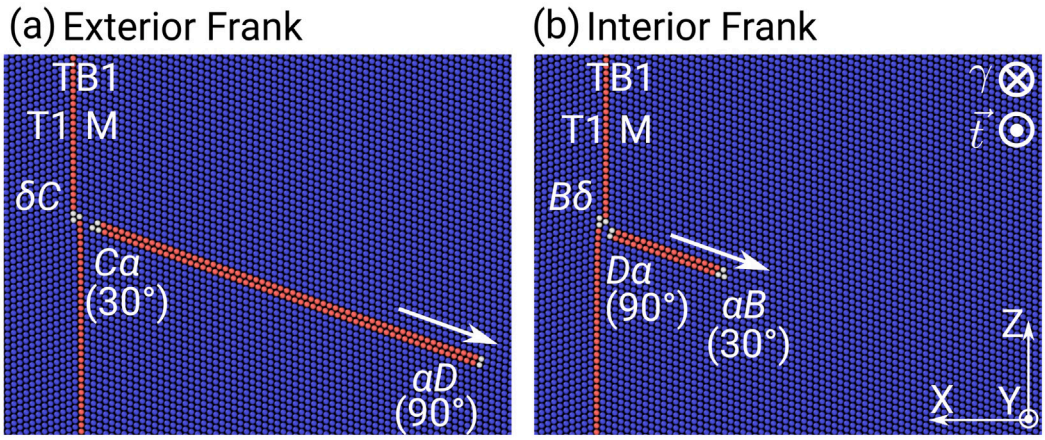

Fig. 4. The dissociation of the relaxed exterior and interior Frank partial dislocations at TB1, shown in Figs. 3(e–f), leads to lattice dislocation emission under applied shear strain γ_{zy}. The glide directions are indicated by white arrows. (a) Dissociation of the stair-rod $\delta\alpha$ ($\frac{1}{6}[\bar{1}0\bar{1}]$) to a 30° trailing Shockley partial $C\alpha$ and a TB Shockley partial δC (Eq. (5)) at $\tau_{zy} \approx 2.22$ GPa. (b) Dissociation of the stair-rod $DB/\alpha\delta$ ($\frac{1}{6}[310]$) to a 90° trailing Shockley partial $D\alpha$ and a TB Shockley partial $B\delta$ (Eq. (6)) at $\tau_{zy} \approx 0.36$ GPa.

a 90° trailing Shockley partial dislocation $D\alpha$ connected by a stacking fault of width ≈ 4.7 nm to the leading Shockley partial dislocation αB. The activation shear stress decreases to $\tau_{zy} \approx 0.25$ GPa at 300 K.

$$\begin{array}{llll} \textbf{Stair-rod}\ DB/\alpha\delta \rightarrow & \textbf{TB Shockley}\ B\delta + & \textbf{Trailing Shockley}\ D\alpha & \\ \frac{1}{6}[310] \quad \rightarrow & \frac{1}{6}[2\bar{1}\bar{1}] \quad + & \frac{1}{6}[121] & \end{array} \tag{6}$$

3.3. Interaction of emitted lattice dislocation with twin boundaries

For both exterior δD and interior $D\delta$ Frank partial dislocations, the dissociation reactions under stress result in 60° lattice dislocations CD or DB with a 90° αD or 30° αB leading Shockley partial dislocation. The further evolution of these 60° lattice dislocations in nanotwinned structures depends on their interaction with the following TBs under simple shear load.

Increasing the shear stress level to $\tau_{zy} \approx 0.46$ GPa, the 30° leading Shockley partial dislocation αB originally emitted from the interior Frank partial dislocation at TB1, is blocked upon encountering TB2. This situation is shown in Fig. 5(a). The leading Shockley partial dislocation αB remains blocked at TB2 upon further increase of the stress. Due to a lack of an effective driving force from the shear component τ_{zy}, the 90° trailing partial dislocation $D\alpha$ does not follow the leading partial. Instead, with increasing shear stress, it glides back toward TB1 (Fig. 5(b)).

At TB1, the trailing partial dislocation $D\alpha$ interacts with the TB Shockley partial dislocation $B\delta$, left behind from the dissociation of the interior Frank partial dislocation in Fig. 4(b), forming a residual dislocation $1/2\,\alpha\alpha^T(1/9\,[111])$, which connects stacking faults across TBs according to the twin symmetry. It remains stable up to an increase of $\tau_{zy} \approx 2.60$ GPa, at which a Shockley partial dislocation is emitted to the left of TB1 (Fig. 5(c)).

The sequence of events resulting from the dislocation of the exterior Frank partial dislocation is more interesting. The Shockley partial dislocation δC in Fig. 4(a) is mobile on TB1 resulting in migration of the TB by one atomic layer, but is not involved in any of the following dislocation-TB interactions (see Supplementary Movie 1 (Fig. F.12)). Fig. 6 shows the time sequence (a) to (h) illustrating the evolution of the lattice dislocation CD with its 90° leading Shockley partial dislocation αD, and its subsequent reactions after interaction with TB2 under shear load. The shear strains γ_{zy} in the time series range from 4.8 to 5.1 %, while the shear stress τ_{zy} remains essentially constant at ≈ 2.24 GPa.

Fig. 6(a) shows the incident lattice dislocation CD with the 90° leading Shockley partial dislocation αD reaching TB2. In Fig. 6(b), the lattice dislocation CD is shown after constriction at TB2 (Eq. (7a)). Next, in image (c), the constricted dislocation core immediately dissociates in a first step into a 30° Shockley partial $B\alpha$ on the matrix side (M) and a 30° Shockley partial $\alpha^T C^T$ on the twin side (T2), leaving a residual dislocation $\alpha B^T/D\alpha^T(1/18[\bar{5}\bar{5}4]^M)$ on TB2 (Eq. (7b)). This residual dislocation is a stair-rod dislocation on TB2, shown in (d), which dissociates further into a 90° Shockley partial αD $(1/6[\bar{1}\bar{2}\bar{1}]^M)$ and a 30° Shockley partial $B^T\alpha^T$ $(1/6[1\bar{1}\bar{2}]^T \Leftrightarrow 1/18[\bar{2}17]^M)$ on two intersected slip planes BCD and $B^TC^TD^T$ in the matrix and twin sides according to Eq. (7c).

Thus, the interaction sequence in Figs. 6 (b–d) results in a 60° lattice dislocation BD re-emitted back on the matrix side (M), and a screw dislocation B^TC^T emitted on the twin side (T2) from TB2. This reaction completes without leaving any residuals on TB2 (Eq. (7d)). Under the applied loading, the re-emitted dislocation BD glides toward TB1.

$$\textbf{On TB2}: \quad C\alpha + \alpha D \rightarrow CD \tag{7a}$$

$$\textbf{On TB2}: \quad CD \rightarrow B\alpha + \alpha^T C^T + \alpha B^T/D\alpha^T \tag{7b}$$

$$\textbf{Residual dissociation}: \quad \alpha B^T/D\alpha^T \rightarrow \alpha D + B^T\alpha^T \tag{7c}$$

$$\textbf{Total reaction}: \quad CD \rightarrow BD + B^TC^T \tag{7d}$$

In Figs. 6 (e–f), the leading 30° Shockley partial dislocation $B\alpha$ glides toward TB1, widening the stacking fault width between it and the 90° trailing partial dislocation αD, which remains almost stationary near TB2. In image (g), the Shockley partial dislocation $B\alpha$ dissociates at TB1 into a 30° Shockley partial dislocation $C^T\alpha^T$ on the twin side (T1) and a residual stair-rod dislocation $\alpha^T\alpha$ $(2/9\,[\bar{1}\bar{1}\bar{1}])$ on TB1 (Eq. (8a)). Subsequently, in image (h), the residual dislocation $\alpha^T\alpha$ on TB1 further dissociates into a 30° Shockley partial dislocation $C\alpha$ on the matrix side (M), completing a CD lattices dislocation and a 30° Shockley partial dislocation $\alpha^T B^T$ on the twin side (T1) (Eq. (8b)).

The reaction sequence of a lattice dislocation BD on TB1 in Figs. 6 (f–h) results in a new lattice dislocation CD of the same type as the initial one in Fig. 6(a) on the matrix side (M) of the twin lamella, and a screw dislocation C^TB^T on the twin side (T1), which glides away from TB1 without leaving any residuals, as described by Eq. (8c).

$$\textbf{On TB1}: \quad B\alpha \rightarrow C^T\alpha^T + \alpha^T\alpha \tag{8a}$$

$$\textbf{Residual dissociation}: \quad \alpha^T\alpha \rightarrow C\alpha + \alpha^T B^T \tag{8b}$$

$$\textbf{Total reaction}: \quad BD \rightarrow CD + C^TB^T \tag{8c}$$

Fig. E.11 shows the shear stress–strain curve for the current loading scenario using periodic boundary conditions along X-axis and rigid

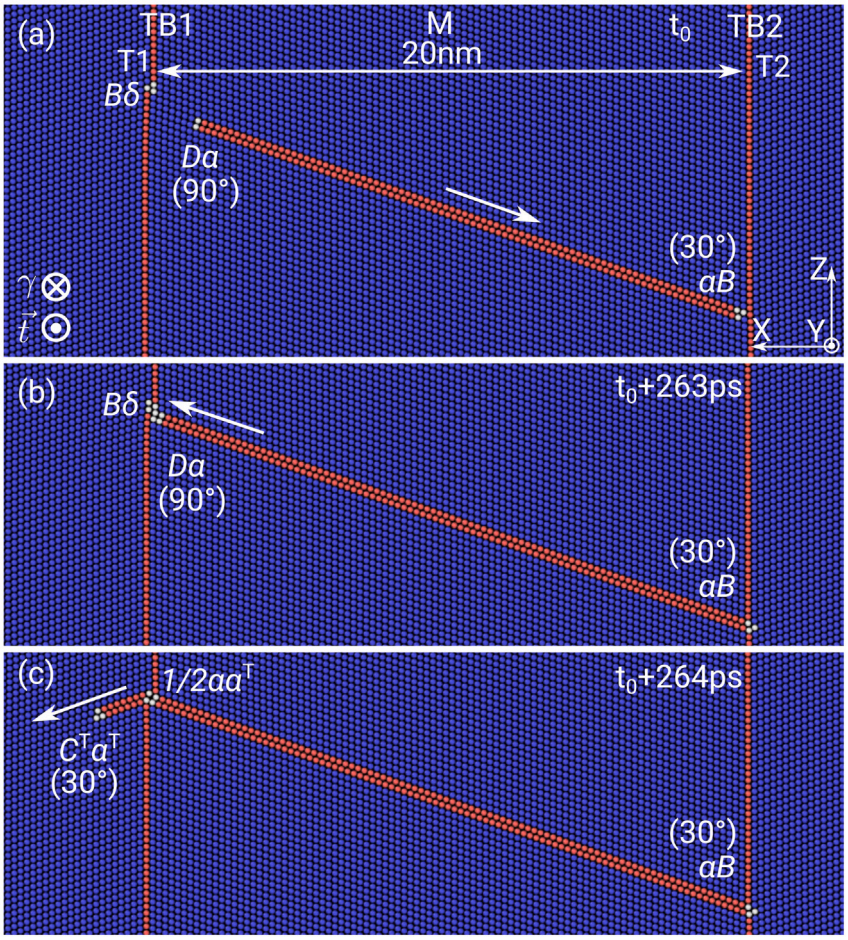

Fig. 5. MD time series of the incident 60° lattice dislocation with a 30° leading Shockley partial dislocation blocked on TB2, originating from the interior Frank partial dislocation. The twin spacing is $\lambda \approx 20\,\text{nm}$ and simple shear γ_{zy} is applied. The glide directions are indicated by white arrows above the stacking faults. (a) An incident lattice dislocation with a 30° leading Shockley partial reaches TB2 ($\tau_{zy} \approx 0.46\,\text{GPa}$). (b) The leading Shockley partial dislocation is still blocked at TB2 ($\tau_{zy} \approx 2.60\,\text{GPa}$) and the partial dislocation $D\alpha$ moves back in the direction of the initial Frank partial dislocation location. (c) The trailing Shockley partial dislocation $D\alpha$ interacting with the TB Shockley partial dislocation $B\delta$ on TB1 forming a residual dislocation $1/2\alpha\alpha^T$ and a transmitted Shockley partial dislocation $C^T\alpha^T$ (slightly increased $\tau_{zy} \approx 2.60\,\text{GPa}$).

boundary conditions. In the periodic case, the shear stress decreases only moderately after the dissociation of the Frank partial dislocation and subsequent dislocation TB transmission & reflection events.

4. Discussion

Frank partial dislocations, often observed as residual defects on TBs, are investigated to understand their energetics and behavior under load. Our molecular dynamics simulations confirm that Frank partial dislocations on TBs can act as "one-time" dislocation sources, consistent with the mechanism proposed by Li et al. [24]. More importantly, we uncover a previously unreported, regenerable dislocation source mechanism involving the transmission & reflection of dislocations at TBs.

4.1. Structure of relaxed frank partial dislocations at TB

Upon energy minimization, exterior and interior Frank partial dislocations on twin boundaries relax into two distinct core configurations. The exterior Frank partial dislocation readily dissociates, leaving a residual $1/6\langle 110\rangle$ stair-rod dislocation at the TB. In contrast, the interior Frank partial dislocation remains compact. Its dissociation would produce a $1/6\langle 130\rangle$ stair-rod dislocation at the TB, which in isotropic elasticity Frank's rule (b^2 criterion) does not appear energetically favorable. These configurations are consistent with atomistic simulation reported for Au [18].

However, our molecular dynamics observations demonstrate that after annealing and subsequent relaxation the interior Frank partial dislocation also remains dissociated. This can be understood with the energetics from anisotropic elasticity (Appendix B) and the barriers associated with the dissociation reactions. For the interior Frank partial dislocation dissociation reaction (Eq. (4)), the energy difference becomes negative, $\Delta E_{\text{pre}}^{\text{aniso}} = -0.26E_0$, in contrast to the positive value using isotropic elasticity $\Delta E_{\text{pre}}^{\text{iso}} = 1.34E_0$ (Table B.2). So the dissociation of the interior Frank partial dislocation is energetically favorable in anisotropic elasticity, consistent with the observed energy reduction upon annealing relaxation (Fig. 3(g)). Furthermore, this suggests that both exterior and interior Frank dislocations are likely to always adopt dissociated configurations at room temperature in experiments.

Although anisotropic elastic analysis suggests that the interior Frank partial dislocation should dissociate, energy minimization at $0K$ shows that it remains compact. This indicates that the dissociation reaction is not barrier-free, and that the dissociation reaction is governed not only by long-range elastic interactions, but also by short-range core effects. To quantify this, we performed CI-NEB calculations and identified a finite energy barrier of $\Delta E \approx 0.095\,\text{eV nm}^{-1}$. At room temperature $T = 300\,\text{K}$, thermal fluctuations provide an energy scale of approximately $0.1\,\text{eV nm}^{-1}$, which is sufficient to activate the dissociation process.

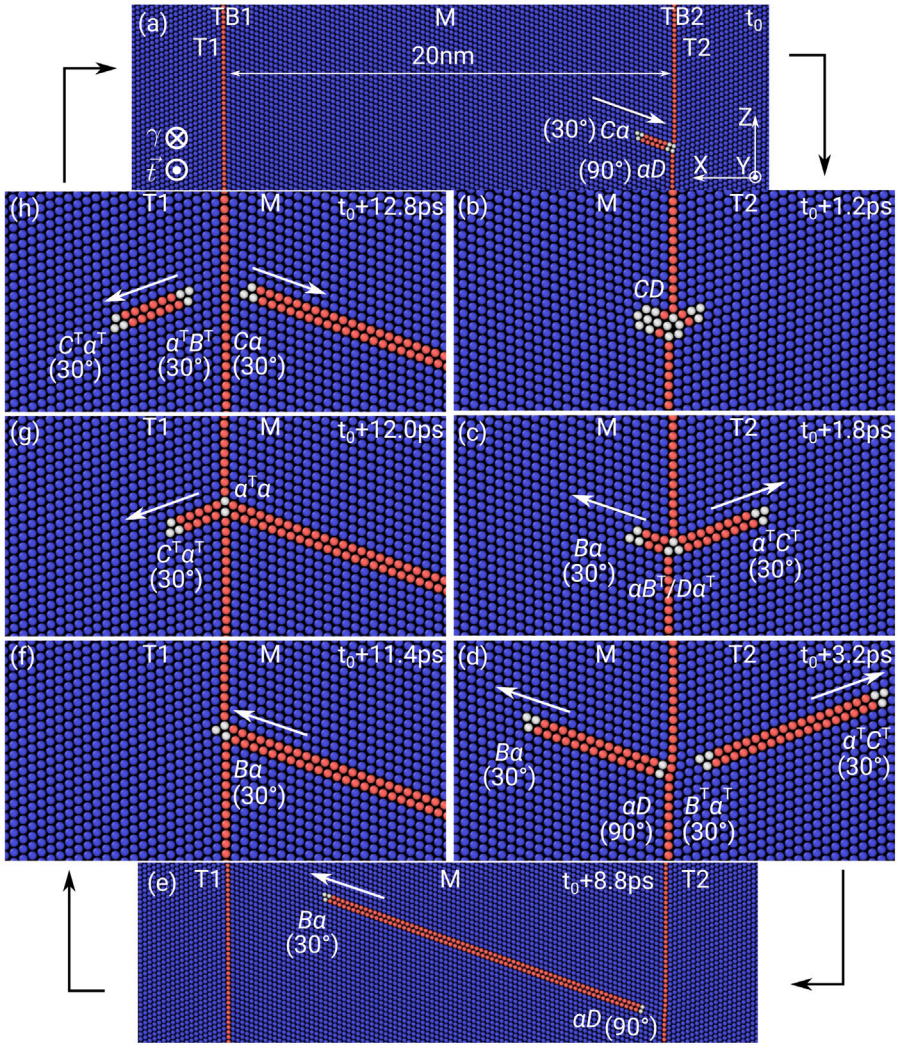

Fig. 6. MD time series of dislocation-TB interactions between a incident 60° lattice dislocation with 90° leading Shockley partial dislocation on TB2 and TB1, originating from the exterior Frank partial dislocation. The twin spacing is $\lambda \approx 20$ nm and simple shear γ_{zy} is applied. The glide directions are indicated by white arrows above the stacking faults. The reaction sequence is in clockwise arrangement indicated by black arrows. A shear stress τ_{zy} of ≈ 2.24 GPa is needed for these dislocation reactions to occur. (a–d) transmission & reflection reaction with dislocation core recombination on TB2. (e–h) transmission & reflection reaction without dislocation core constriction on TB1.

The elastic strain energies of the dissociated Frank partial dislocations, extracted from the atomistic data (Fig. 3(h)) are in excellent agreement with the expected anisotropic elasticity prefactor value (Appendix C). The energy difference between the two Frank partial dislocation types can be attributed to the dislocation core energies. It is noteworthy that the core energy of the interior Frank partial dislocation is significantly larger than that of the exterior type.

4.2. Frank partial dislocation dissociation under load

Under applied shear, we observe that a mobile non-screw lattice dislocation can be emitted from both Frank partial dislocation types with a mobile TB Shockley partial dislocation, as summarized in Eq. (9) with line direction $\vec{l} = BC$. The emitted lattice dislocation with both the slip plane and Burgers vector inclined to TBs can glide toward the adjacent TBs and a high stress is required to activate the dislocation-TB interactions, while the glide of the TB Shockley partial dislocation with the migration of TBs can result in detwinning process with much lower stress [40,42,43].

However, the activation shear stress τ_{zy} for lattice dislocation emission from the dissociated exterior Frank partial dislocation (2.22 GPa) is much higher than the one required for the interior Frank partial dislocation (0.36 GPa).

$$\textbf{Exterior Frank } \delta D \rightarrow \quad \textbf{TB Shockley } \delta C + \quad \textbf{Lattice } (C\alpha + \alpha D)$$
$$\frac{1}{3}[\bar{1}\bar{1}\bar{1}] \quad \rightarrow \quad \frac{1}{6}[11\bar{2}] \quad + \quad \frac{1}{2}[\bar{1}\bar{1}0] \tag{9a}$$
$$\textbf{Interior Frank } D\delta \rightarrow \quad \textbf{TB Shockley } B\delta + \quad \textbf{Lattice } (D\alpha + \alpha B)$$
$$\frac{1}{3}[111] \quad \rightarrow \quad \frac{1}{6}[2\bar{1}\bar{1}] \quad + \quad \frac{1}{2}[011] \tag{9b}$$

The large differences in the required stresses are consistent with the anisotropic energy difference for the dissociation reactions for the respective stair-rod dislocations: $9.26E_0$ for the $1/6\langle 110\rangle$ stair-rod dislocation (exterior) and $2.54E_0$ for the $1/6\langle 130\rangle$ stair-rod dislocation (interior), as listed in Table B.2. Furthermore, the significantly larger core energy of the interior Frank partial dislocation promotes its dissociation, as the system can lower its total energy more effectively through core reconfiguration compared to the exterior type.

For the exterior Frank partial dislocation, the resolved shear stress for emission of the 30° trailing Shockley partial dislocation $C\alpha$, to form a fully mobile lattice dislocation, from the $1/6\langle 110\rangle$ stair-rod dislocation

dissociation is $\tau_{rss} \approx 1.8\,\text{GPa}$[1] at 0.1 K and decreases slightly to 1.5 GPa at 300 K. The MD simulation results, obtained for idealized simple shear load and high strain rate of ($\sim 10^8\,\text{s}^{-1}$), are close to reported experimental activation stresses of 1.6 GPa [24] and 1.87 GPa [17], which are estimated from the maximum shear stress from Hertzian contact mechanics beneath a nanoindenter [24] and the mean shear strain near the step [17]. The high strain rate may lead to an overestimation of the activation stress but the dissociation reaction is expected to follow the same reaction path [44,45]. Both, molecular dynamics and experimental results, demonstrate the ability of TB Frank partial dislocations to act as dislocation sources at TBs requiring a high activation stress.

4.3. Stability of frank partial dislocation at TB

The dissociated exterior Frank partial dislocation is commonly observed in experiments as a $1/6\langle 110\rangle$ stair-rod dislocation on TBs, connected to an emitted 90° Shockley partial dislocation [20,46]. The dissociated interior Frank partial dislocation with the emitted 30° Shockley partial dislocation has been observed experimentally in isolated cases [47]. The relative scarcity of experimental observations of interior Frank partial dislocations can be rationalized by the intrinsic instability of interior Frank partial dislocations based on our atomistic results and energy analysis detailed in Table B.2.

The atomistic result shows that a lattice dislocation is emitted from the interior Frank partial dislocation at low stress levels. The dissociation energy barrier of a $1/6\langle 130\rangle$ stair-rod dislocation is $2.54E_0$ using anisotropic elasticity estimates. A dissociated interior Frank partial dislocation can be formed via the interaction of lattice dislocation with a 90° leading Shockley partial dislocation αD and a TB, following the reaction αD (90°) $\rightarrow$ $\delta\alpha/CD$ ($1/6\langle 130\rangle$) + $C\delta$ (30°). This formation energy barrier ($10.18E_0$) is much higher than the dissociation energy barrier ($2.54E_0$). Thus, the interior Frank partial dislocation is intrinsically unstable and tends to dissociate and emit a lattice dislocation at a relatively low stress level.

After the dissociation of an interior Frank partial dislocation a lattice dislocation with a 30° leading Shockley partial dislocation is emitted. Once the leading partial dislocation encounters the neighboring TB, a $1/6\langle 110\rangle$ stair-rod dislocation is formed [48,49]. This stair-rod dislocation connected by a SF to the 90° trailing dislocation corresponds to the exterior Frank partial dislocation in Fig. 3(e). The energy barrier of the associated reaction αB (30°) $\rightarrow$ $\alpha\delta$ ($1/6\langle 110\rangle$) + δB (30°) is $3.46E_0$ and is only slightly larger than the dissociation energy of a $1/6\langle 130\rangle$ stair-rod dislocation ($2.54E_0$). As the energy barrier of $9.26E_0$ for further dissociation of the $1/6\langle 110\rangle$ stair-rod dislocation is large, the exterior Frank partial dislocation is rather stable.

Therefore, the interior Frank partial dislocation is not likely to be found at TBs. In contrast, the exterior Frank partial dislocation is more stable, having a higher dissociation energy than its formation energy, and a lower core energy. This is consistent with the observation of Frank partial dislocations on TB showing a characteristic compression and dilatation pattern compatible with relaxed exterior Frank partial dislocations [20,50]. The presence of only one type of Frank partial dislocation also leads to the reported misorientation increase with increasing defect density [20,50,51].

[1] The resolved shear stress τ_{rss} is converted from the applied shear stress $\tau_{zy} \approx 2.22\,\text{GPa}$ on $Z-$plane ($\vec{n}_Z \parallel [\bar{1}2\bar{1}]$) along $-Y$ direction ($-Y \parallel [\bar{1}01]$) on the 30° trailing Shockley partial dislocation $\vec{b}_{C\alpha} = [\bar{2}\bar{1}1]/6$ on glide plane BCD ($\vec{n}_{\text{BCD}} = [\bar{1}1\bar{1}]/\sqrt{3}$) with the ratio of $\tau_{rss}/\tau_{zy} = \cos\angle(n_Z, \vec{n}_{\text{BCD}})\cos\angle(-Y, \vec{b}_{C\alpha})$.

4.4. Cooperative transmission & reflection of dislocations at TBs

The dislocation-TB interactions in Eqs. (7) and (8) have in common to generate a reflected lattice dislocation to the incident side and a screw lattice dislocation on the transmission side: it is a dislocation cooperative transmission & reflection mechanism with dislocation multiplication. The transmission & reflection mechanism without lattice dislocation constriction in Eq. (8) was previously observed in MD simulations [52–54], while the dissociation of an incident lattice dislocation after combination and constriction on both incident and transmission sides in Eq. (7) is the newly uncovered mechanism.

The overall occurrence of these multiplication reactions is governed by the largest energy differences among the intermediate steps in Eqs. (7) and (8), which correspond to Eqs. (7a) and (8a) given in Table B.2. Although these energy differences are relatively large, they are similar to the one for the dissociation of a $1/6\langle 110\rangle$ stair-rod dislocation in Eq. (5). Therefore, the required shear stress for the emission of a lattice dislocation from the dissociated exterior Frank partial dislocation should also be sufficient to activate the transmission & reflection mechanisms.

Different cooperative transmission & reflection reactions have been experimentally observed and identified as a cooperative movement of three sets of dislocations (incident/reflected/transmitted) from dynamic in situ loading tests [55–58]. Although the incident and reflection slip planes are not identical because of the incident dislocation pile-ups rather than a single dislocation, this process is observed to be repeated several times for incident pile-ups approaching a TB.

In addition to the energy barrier, dislocation interactions with TBs depend on the loading condition. A screw dislocation can in principle be transmitted across TBs via cross-slip, while transmission of a dislocation with an edge component requires nucleation of a TB dislocation [39,40]. If the latter nucleation is suppressed due to insufficient shear stress on the TB, the incident 60° dislocation is reflected as another 60° dislocation. The incident dislocation (with Burgers vector $CD \rightarrow C\alpha + \alpha D$) and the reflected dislocation (with Burgers vector $BD \rightarrow B\alpha + \alpha D$) differ only in their flipped screw component: $C\alpha \rightarrow B\alpha + B^{\text{T}}C^{\text{T}}$. The backward glide of the reflected dislocation is driven by the externally applied shear loading along CB, which leads to resolved shear stresses on the 30° Shockley partial dislocation $B\alpha$ but not on the 90° one αD.

The scenario discussed in this paper uses symmetric simple shear load along the dislocation line direction of an infinite long straight dislocation in a quasi-two dimensional setup. A fully three dimensional situation allows for more nucleation scenarios and thus the activation stresses in the current setup could be higher than in a fully three dimensional setup but the fundamental interaction mechanisms are expected to be unaffected [59].

4.5. Dislocation source mechanism in a twin lamella

In nanotwinned structures, the observed cooperative transmission & reflection mechanisms act in concert (Fig. 6, Eqs. (7) and (8)) leading to the continuous emission of screw dislocations from neighboring twin boundaries. This new source mechanism, illustrated schematically in Fig. 7, operates as a two-step process: initial nucleation of a lattice dislocation at the TB is followed by repeatable transmission & reflection reactions across adjacent twins.

1. Nucleation of a lattice dislocation: The process is initiated by the complete dissociation of a Frank partial dislocation F, which results in the emission of a 60° lattice dislocation L_0 from the initial TB1 gliding toward the neighboring TB2 as illustrated in Fig. 7(a). The Frank partial dislocation F is destroyed after emitting L_0 and a mobile TB Shockley partial dislocation, which is not participating in any of the subsequent steps of the mechanism.

$$\textbf{Frank F} \rightarrow \textbf{Lattice L}_0 + \textbf{TB Shockley} \tag{10}$$

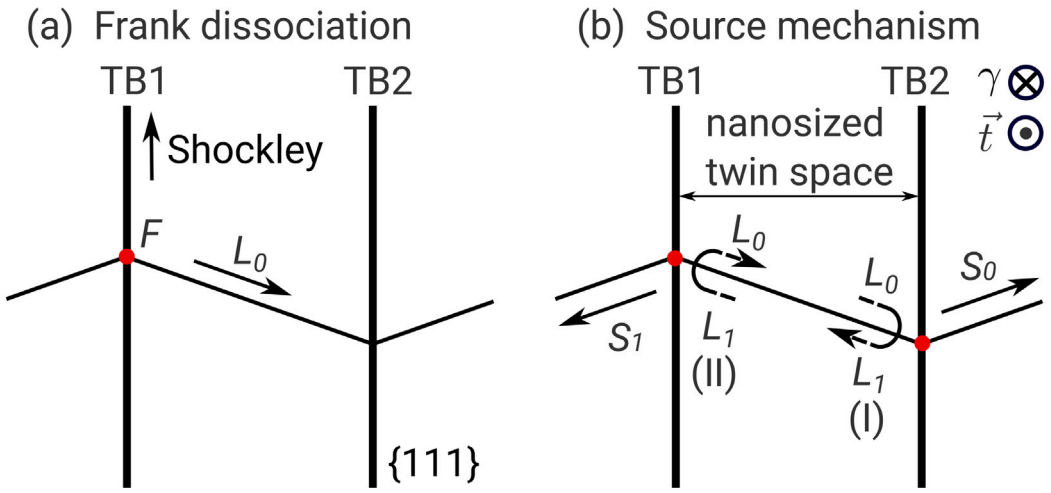

Fig. 7. Schematic illustration of the dislocation source mechanism in FCC nanotwinned structure with simple shear γ parallel to dislocation line direction $\vec{t} = \langle 110 \rangle$. Glide direction is indicated by arrow. (a) Lattice dislocation L_0 emitted from the dissociation of Frank partial dislocation F. (b) Lattice dislocation L_0 and L_1 are reflected between TB1 and TB2 with the consequently emitting screw lattice dislocation S_0 and S_1.

2. Source mechanism:

   (I) The lattice dislocation L_0 interacts with TB2, inducing the re-emission of a new 60° lattice dislocation L_1, that glides back toward TB1. Concurrently, a screw dislocation S_0 is transmitted through TB2. No residual dislocation is left at TB2.

   $$60^\circ \textbf{ Lattice } \mathbf{L_0} \rightarrow 60^\circ \textbf{ Lattice } \mathbf{L_1} + \text{Screw } \textbf{Lattice } \mathbf{S_0}$$

   (II) Once L_1 interacts with TB1, a second re-emission event on TB1 results in a dislocation of type L_0 and a transmitted S_1 screw dislocation. No residual dislocation is left at TB1 either.

   $$60^\circ \textbf{ Lattice } \mathbf{L_1} \rightarrow 60^\circ \textbf{ Lattice } \mathbf{L_0} + \text{Screw } \textbf{Lattice } \mathbf{S_1}$$

   The steps (I) and (II) form a repeatable process: with each repetition a screw dislocation pair S_0 and S_1 with inverse Burgers vector but same line directions are emitted from the (nanosized) twin lamella limited by TB1 and TB2 in Fig. 7(b).

The initial Frank partial dislocation is one possible source of a 60° lattice dislocation L_0 parallel to the TBs to activate the proposed continuous source mechanism. Frank partial dislocations can be intrinsic defects at TBs [22,23] or resulting from dislocation-TB interactions [7,15]. More generally speaking, defective twin boundaries, i.e. steps at TBs, can potentially trigger dislocation emission due to stress concentration [5,17]. A 60° lattice dislocation can also originate from a transmitted dislocation [15,40]. Nevertheless, a high stress level is needed to activate the 60° lattice dislocation emission or transmission, which is also sufficient to activate the two cooperative transmission & reflection reactions, as shown in the stress–strain curve (Fig. E.11). The shown strain range covers the Frank partial dislocation dissociation leading to an initial lattice dislocation L_0 and multiple source activations at an almost constant shear stress level. The repeatable source mechanism can be disturbed by the emitted screw dislocations due to the periodic boundary conditions. The Supplementary Movie 1 (Fig. F.12) shows for rigid fixed boundary conditions in the dislocation emission direction, three cycles of $L_0 \rightarrow L_1$ on TB2, then $L_1 \rightarrow L_0$ on TB1. Note that, in the absence of preexisting defects or lattice dislocations, the deformation of nanotwinned structures exhibits a pronounced stress drop following dislocation nucleation from the sample surface [52].

This source mechanism enables sustained dislocation activity within the nanotwinned structure, and serves as an efficient screw dislocation source. A single source leads to localized deformation with a saw-tooth like signature. However assuming multiple 60° lattice dislocations nucleated at different locations (Frank partial defects) within the twinned structure, it can undergo plastic deformation while maintaining a high flow stress.

The newly identified screw dislocation source mechanism, when operating continuously and rapidly enough to accommodate external loading, would limit further hardening once the activation stress is reached, because TBs cannot act as strong barriers for screw dislocations [39,60] and the formation of pile-ups is suppressed in nanosized twin lamellar. In this study, additional dislocations at TBs, e.g. TB Shockley partials, as reaction partners are not considered, leaving potential hardening mechanisms open to be explored in future studies. The detailed hardening behavior is expected to depend on the density of reaction partners on the TB [61].

Previous studies on dislocation-TB interactions involving either pure screw or 60° dislocations shows dislocations may or may not transmit across the TB with residual dislocations [39,40]. This indicates that dislocation-TB interactions depends on the loading conditions and less symmetric loading conditions can result in more complex reaction products. Preliminary studies (Supplementary Video 2 (Fig. F.13)) shows a sample with the twin boundaries rotated by 20° around the Y axis of the simulation cell, while applying the same simple shear loading. The new source mechanism still works to continuously emit screw dislocations ($\gamma_{zy} \sim 4.72\%$ which leads to $\tau_{zy} \sim 2.14\,\text{GPa}$) when deviating significantly from the symmetrical loading scenario.

The emitted screw dislocations can follow two competing mechanisms, direct transmission or absorption on TBs, under the influence of loading conditions [39,59,62,63]. Moreover, absorption is the preferable mechanism for perfect TB without preexisting dislocations [61]. Therefore, the new screw dislocation source mechanism can also contribute to the TB Shockley partial dislocation density, leading to TB migration and thus to detwinning [49,64,65].

Finally, we will discuss the implications of the newly identified screw dislocation source mechanism for strategies aiming at enhancing strength without severely compromising ductility in nanotwinned metals [6]. In this study, a twin spacing of 20 nm is used, permitting the dissociation of both types of Frank partial dislocations and the formation of an unstable dislocation source, since a TB Frank partial dislocation can only emit one TB Shockley partial dislocation and one lattice dislocation. For larger twin spacings, the cooperative transmission & reflection reactions are not expected to alter if only a single

lattice dislocation is trapped in twin lamella. At smaller twin spacings ($\lambda \sim 10\,\text{nm}$), although such small twin spacings enhance the reflection frequency of lattice dislocation (Fig. 7(b)), the TB Shockley partial dislocation emission from the TB/GB junctions are reported to becomes the dominant dislocation source and results in softening [8,17,66].

This finding suggests the existence of an optimal twin spacing (λ in $10 \sim 20\,\text{nm}$) for a strength–ductility synergy of nanotwinned metal compatible with a high TB dislocation density with the high stress activated dislocation-TB interactions instead of easy glide of TB Shockley partial dislocations along TBs. Dislocation interactions between hard mode (TB transverse direction) and soft mode (TB glide direction) deformation can create temporary sessile TB dislocations, e.g. stair-rod dislocations, which will dissociate further due to stress concentration to prevent strain localization. Thus, the nanosized twin thickness elevates work hardening from the interactions between different slip systems without sacrificing ductility.

5. Conclusion

The energetics and stability of two types of Frank partial dislocation, exterior and interior, are investigated as defects on twin boundaries. We confirm that Frank partial dislocation can act as a "one-time" twin boundary dislocation source. Moreover, we identify a stable, regenerable dislocation source mechanism operative in nanotwinned structures. The key findings are as follows:

1. After annealing relaxation, both Frank partial dislocation types are dissociated, in agreement with anisotropic elasticity and experimental observation.
2. The difference in total energy of the two types of Frank partial dislocation arises from their core energies. The interior Frank partial dislocation has a much higher core energy.
3. Frank partial dislocations located on TBs can act as "one-time" sources, emitting a 60° lattice dislocation and a mobile TB Shockley partial dislocation.
4. The activation stress from atomistic simulations for lattice dislocation emission from the exterior Frank partial dislocation agrees with the experimentally reported pop-in stresses in twinned Cu [24].
5. Two cooperative transmission & reflection mechanisms with and without lattice dislocation constriction are identified for the dislocation–twin boundary interaction: an incident 60° dislocation results in a reflected 60° dislocation and a transmitted screw dislocation, while details, e.g. intermediate constriction, depend on the partial dislocation order.
6. A new stable source mechanism in nanotwinned structures is uncovered: A 60° lattice dislocation confined within a twin lamella, e.g. nucleated from a Frank partial dislocation, can act as a continuous dislocation source under shear load perpendicular to the twin plane. This mechanism operates via successive cooperative transmission & reflection processes at adjacent twin boundaries, resulting in the emission of screw dislocations on both sides of the twin lamella. Preliminary tests show that the source mechanism remains active under significantly asymmetric loading.

The identification of a new, stable dislocation source reveals a previously overlooked multiplication mechanism that may help explain the exceptional ductility of nanotwinned materials.

CRediT authorship contribution statement

D. Liu: Writing – review & editing, Writing – original draft, Visualization, Methodology, Investigation, Formal analysis, Data curation, Conceptualization. **D. Weygand:** Writing – review & editing, Writing – original draft, Validation, Supervision, Project administration, Methodology, Investigation, Conceptualization. **J. Li:** Conceptualization. **C. Kirchlechner:** Writing – review & editing, Supervision, Conceptualization. **P. Gumbsch:** Writing – review & editing, Supervision, Resources, Funding acquisition, Conceptualization.

Declaration of competing interest

The authors declare that they have no known competing financial interests or personal relationships that could have appeared to influence the work reported in this paper.

Acknowledgment

The authors acknowledge support by the state of Baden-Württemberg through bwHPC.

Appendix A. The dependence of the stacking fault width on twin spacing and frank dipole separation distance

Fig. A.8 shows the dependency of the width of the stack fault d_{SF} on twin spacing λ and Frank dipole separation distance d after annealing relaxation. In Fig. A.8(a), the stacking fault width d_{SF} for the exterior Frank partial dislocation increases as the separation distance decreases. A stable stacking fault width of $d_{\text{SF}} \approx 2.3\,\text{nm}$ is reached for $\lambda \geq 5\,\text{nm}$ and $d \geq 30\,\text{nm}$. Fig. A.8(b) shows that the stacking fault width of $d_{SF} \approx 1.1\,\text{nm}$ converges for $\lambda \geq 10\,\text{nm}$ and is independent of the separation distance d for the interior Frank partial dislocation. When the twin spacing λ approaches the width of the stack fault, as shown in the insets of the figures, the expanding stack fault can be blocked by the adjacent TB. For $\lambda \geq 10\,\text{nm}$ and $d \geq 30\,\text{nm}$, both types of Frank partial dislocations exhibit a stable stacking fault width.

Appendix B. The anisotropic and isotropic elastic energy of dislocations and dislocation reactions

The elasticity coefficient K^{aniso} is calculated using the sextic formalism of Stroh in anisotropic elasticity with the elastic constants C_{11}, C_{12} and C_{44} [28]. In Eq. (B.1), the prime denotes elastic constant transformed into the samples coordinate system, where the dislocation line direction is along $[10\bar{1}]$ (see Fig. 1). For comparison, the isotropic elastic coefficient K^{iso} is calculated from the shear modulus of copper $G = 48\,\text{GPa}$, Poisson's ratio $\nu = 0.34$, and the angle β between the Burgers vector and the line direction.

$$K^{\text{aniso}} = K(C'_{11}, C'_{12}, C'_{44}) \tag{B.1}$$

$$K^{\text{iso}} = G\frac{1-\nu\cos^2\beta}{1-\nu} \tag{B.2}$$

To simplify the presentation of the results as tables, the prelogarithmic energy factor E_{pre} in Eq. (2) is expressed as $E_{\text{pre}} = \frac{K}{G}b^2E_0$, in terms of the ratio of elasticity coefficient and shear module K/G, the squared magnitude of the Burgers vector b^2 in units of $a^2/36$ and $E_0 = \frac{G}{4\pi}\frac{a^2}{36} \approx 0.087\,\text{eV nm}^{-1}$. The lattice constant is $a = 3.615\,\text{Å}$. Applying this notion for the Frank partial dislocation $D\delta$ $(1/3[111])$, the anisotropic pre-logarithmic energy factor is $E^{\text{aniso}}_{\text{pre}} = \frac{K}{G}b^2E_0 = 19.92E_0$ with $K^{\text{aniso}}/G = 79.55\,\text{GPa}/48\,\text{GPa} = 1.66$ and $b^2 = 12$ in units of $a^2/36$. The pre-logarithmic elastic energy factors using isotropic and anisotropic elasticity are summarized in Table B.1, limited to dislocation types relevant to the current study.

The anisotropic and isotropic energy differences for relevant dislocation reactions $\Delta E_{\text{el}} = E_{\text{product}} - E_{\text{reactant}}$, summarized in Table B.2, are calculated by subtracting the elastic energy pre-factors of the reactant dislocations from that of the product.

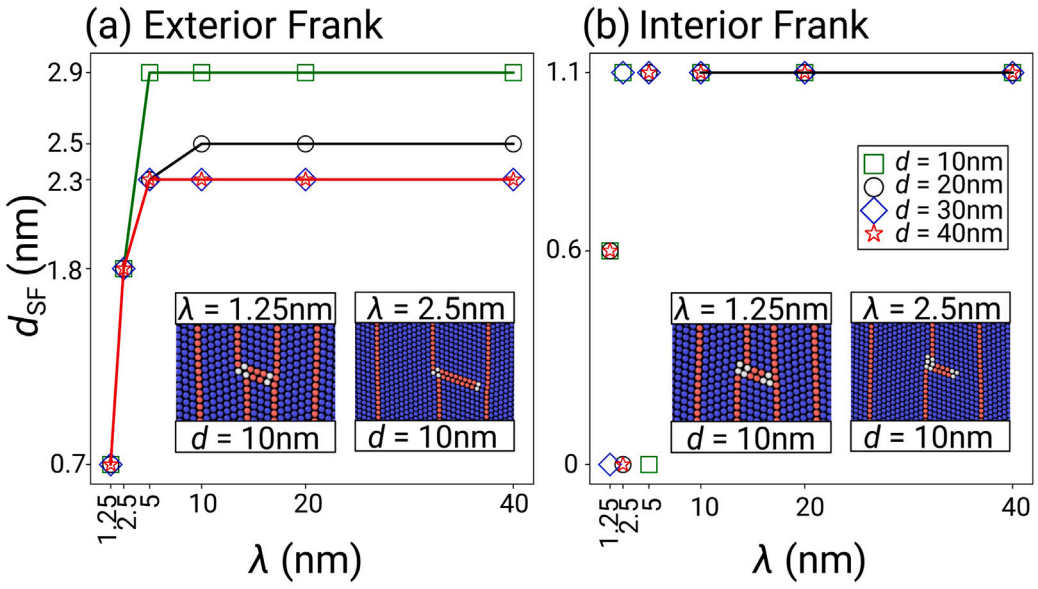

Fig. A.8. Dependence of stacking fault width d_{SF} on twin spacing λ and Frank partial dislocation dipole separation distance d for both Frank partial dislocation types after annealing relaxation. (a) The exterior Frank partial dislocation reaches a stable stacking fault width of $d_{SF} \approx 2.3$ nm for $\lambda \geq 5$ nm and $d \geq 30$ nm. (b) The interior Frank partial dislocation reaches a stable stacking fault width of $d_{SF} \approx 1.1$ nm for $\lambda \geq 10$ nm and independent on d.

Table B.1
The anisotropic and isotropic elastic energy of dislocations.

Dislocations	b [a]	b^2 [$a^2/36$]	K^{aniso}/G	E_{pre}^{aniso} [E_0]	K^{iso}/G	E_{pre}^{iso} [E_0]
Frank $D\delta$	1/3 [111]	12	1.66	19.92	1.52	18.24
Stair-rod $\delta\alpha$	1/6 $[\bar{1}0\bar{1}]$	2	1.73	3.46	1.52	3.04
Stair-rod $DB/\alpha\delta$	1/6 [310]	10	1.33	13.30	1.28	12.80
Stair-rod $\alpha^T\alpha$	2/9 $[\bar{1}\,\bar{1}\,\bar{1}]$	5.33	1.66	8.85	1.52	8.10
Stair-rod $\alpha B^T/D\alpha^T$	1/18 $[\bar{5}\bar{5}4]$	7.33	1.13	8.28	1.20	8.80
30° Shockley αB	1/6 $[\bar{1}12]$	6	1.06	6.36	1.13	6.78
90° Shockley αD	1/6 $[\bar{1}2\bar{1}]$	6	1.58	9.48	1.52	9.12
60° lattice CD	1/2 $[\bar{1}\bar{1}0]$	18	1.41	25.38	1.39	25.02

$G = 48$ GPa, $C_{11}, C_{12}, C_{44} = 169.9, 122.6, 76.2$ GPa [26] $\quad E_0 = \frac{G}{4\pi}\frac{a^2}{36}$

Table B.2
The anisotropic and isotropic elastic energy differences for dislocation reactions.

Description	Reactions	Eq. #	ΔE_{pre}^{aniso} [E_0]	ΔE_{pre}^{iso} [E_0]
Exterior Frank relaxation	$\delta D \rightarrow \delta\alpha + \alpha D$	(3)	−6.98	−6.08
Interior Frank relaxation	$D\delta \rightarrow DB/\alpha\delta + \alpha B$	(4)	−0.26	1.34
1/6⟨110⟩ Stair-rod dissociation	$\delta\alpha \rightarrow \delta C + C\alpha$	(5)	9.26	10.52
1/6⟨130⟩ Stair-rod dissociation	$DB/\alpha\delta \rightarrow D\alpha + B\delta$	(6)	2.54	3.10
Dislocation constriction	$C\alpha + \alpha D \rightarrow CD$	(7a)	9.54	9.12
Transmission & reflection	$CD \rightarrow B\alpha + \alpha^T C^T + \alpha B^T/D\alpha^T$	(7b)	−4.38	−2.65
Transmission & reflection	$\alpha B^T/D\alpha^T \rightarrow \alpha D + B^T\alpha^T$	(7c)	7.56	7.09
Transmission	$B\alpha \rightarrow C^T\alpha^T + \alpha^T\alpha$	(8a)	8.85	8.10
Transmission & reflection	$\alpha^T\alpha \rightarrow C\alpha + \alpha^T B^T$	(8b)	3.87	5.46
1/6⟨110⟩ Stair-rod formation[a]	αB (30°) $\rightarrow \alpha\delta + \delta B$	Zhu et al. [48]	3.46	3.04
1/6⟨130⟩ Stair-rod formation[b]	αD (90°) $\rightarrow \delta\alpha/CD + C\delta$	plausible	10.18	10.46
90° Shockley dissociation[c]	αD (90°) $\rightarrow \alpha\delta + \delta D$	Zhu et al. [48]	13.90	12.16

[a] Alternative reaction: $C\alpha \rightarrow \delta\alpha + C\delta$ corresponding to the configuration in Fig. 3 (e).
[b] Alternative reaction: $D\alpha \rightarrow DB/\alpha\delta + \delta B$ corresponding to the configuration in Fig. 3 (f).
[c] Alternative reaction of 90° Shockley partial dislocation on TBs associated with an even higher energy barrier.

Appendix C. The dislocation dipole and quadrupole configuration for dislocation energy calculation

Table C.3 summarizes the results for the dipole configuration ($d, \lambda \approx 40$ nm) and the quadrupole configuration ($d, \lambda \approx 40$ and 80 nm). The reported values are:

- the ratio of estimated to ideal TB energy $\gamma_{TB}/\gamma_{TB}^{ideal}$
- the elasticity coefficients K (GPa) from the measured prelogarithmic energy factor
- the core energy E_c (eV nm^{-1})
- the core energy difference $E_c^{int} - E_c^{ext}$ between the interior and exterior Frank partial dislocations

In the dipole configuration, the twin boundary energy exceeds the ideal value due to a strain of at most 0.26%, which results from the

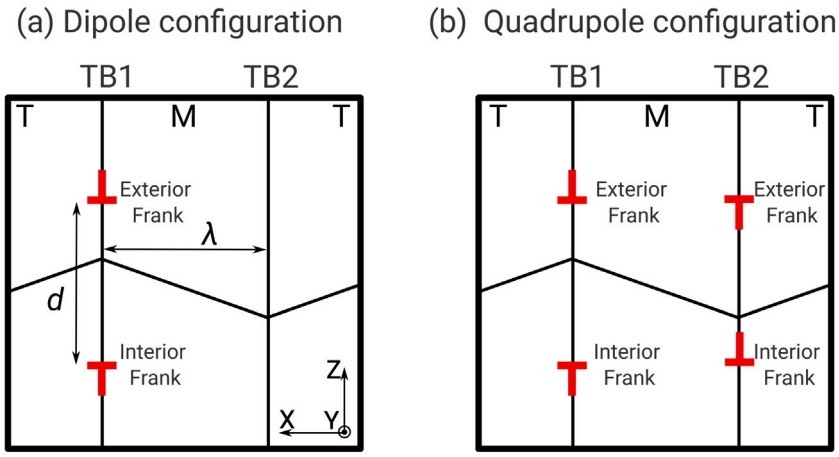

Fig. C.9. The dislocations and twin boundaries are arranged in a dipole configuration in (a), created by removing one atomic layer adjacent to the TB between the two Frank partial dislocations. To restore periodicity and eliminate constraints, an additional dipole of opposite sign is introduced on the neighboring TB in (b), forming a quadrupole configuration.

Table C.3
Dipole and quadrupole configurations: Ratio of estimated to ideal TB energy $\gamma_{TB}/\gamma_{TB}^{ideal}$, elasticity coefficients K (GPa) from atomistic data, core energy E_c (eV nm^{-1}) and core energy difference are summarized for the exterior and interior Frank partial dislocations.

Configuration	Type	$\gamma_{TB}/\gamma_{TB}^{ideal}$	K	E_c	$E_c^{int} - E_c^{ext}$
Dipole	Exterior	1.159	79.19	0.226	1.701
$d, \lambda \approx 40$ nm	Interior	1.144	79.71	1.927	
Quadrupole	Exterior	1.075	79.76	0.229	1.777
$d, \lambda \approx 40$ nm	Interior	1.052	79.62	2.006	
Quadrupole	Exterior	1.015	79.56	0.365	1.741
$d, \lambda \approx 80$ nm	Interior	1.012	79.36	2.106	

removal of one atomic layer out of 384 between the dislocation dipole. In the quadrupole configuration, overall no atomic layer is missing, and the twin boundary energy closely matches the ideal value at $d, \lambda \approx 80$ nm. In all configurations, the prelogarithmic energy factor for both Frank partial dislocations on the twin boundary agrees well with the anisotropic elasticity value $K^{aniso} = 79.55$ GPa. Although the absolute core energy E_c shows some dependence on size and configuration details, the difference in core energy between both dislocation types remains consistently significant (≈ 1.740 eV nm$^{-1} \pm 3\%$).

Appendix D. TB energy contribution estimation

To access the dislocation core energy from the atomistic results, the following scheme is employed: We estimate the twin boundary energy contribution by calculating the dislocation elastic energy E_{el} using the pre-logarithmic energy factor $E_{pre} = K^{aniso} b^2/4\pi$ as detailed in Appendix B. For dislocations parallel to the twin boundary, E_{pre} remains identical to its bulk value, and no image forces arise due to the twin orientation relation. This is a particular property for the twin misorientation relation also confirmed by numerical evaluation of interfacial energy prefactors [60,67].

By subtracting the cohesive and elastic energy terms from Eq. (1), the remaining energy per unit dislocation length is expressed as a linear function of the cylinder radius R, where the slope corresponds to twice the twin boundary energy $2\gamma_{TB}$ and the intercept yields the core energy:

$$(E_{tot}(R) - N(R)E_{coh})/L - E_{el}^{aniso}(R, r_c) = E_{TB}(R, \gamma_{TB})/L + E_c(r_c) = 2R\gamma_{TB} + E_c(r_c) \quad (D.1)$$

The sum of the TB energy and the core energy from the atomic simulations is found to be linearly proportional to R in Fig. D.10. The estimated TB energy per unit area γ_{TB} is derived from the two slopes

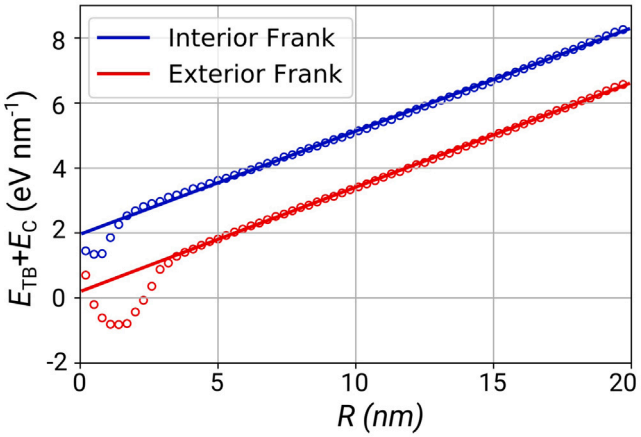

Fig. D.10. Dependence of the TB energy $E_{TB}(R)$ per length and core energy E_c as function of the outer cylinder radius R calculating the elastic energy E_{el} in Eq. (D.1) using the anisotropic elasticity coefficient $K^{aniso} = 79.55$ GPa (see Appendix B).

$2\gamma_{TB}$ for R in the range 5 to 20 nm leading to $\gamma_{TB}^{ext} \approx 1.159\gamma_{TB}^{ideal}$ and $\gamma_{TB}^{int} \approx 1.144\gamma_{TB}^{ideal}$. The linear regressions used to find the prelogarithmic energy factor E_{pre} (Fig. 3(h)) and the TB energy γ_{TB} (Fig. D.10) have coefficients of determination of $R^2 > 0.997$, showing an excellent fit.

The observed linear behavior confirms the assumptions of independent Frank partial dislocations and uniform twin boundary energy in presence of the Frank partial dislocations and spurious normal stresses due to the periodic boundary.

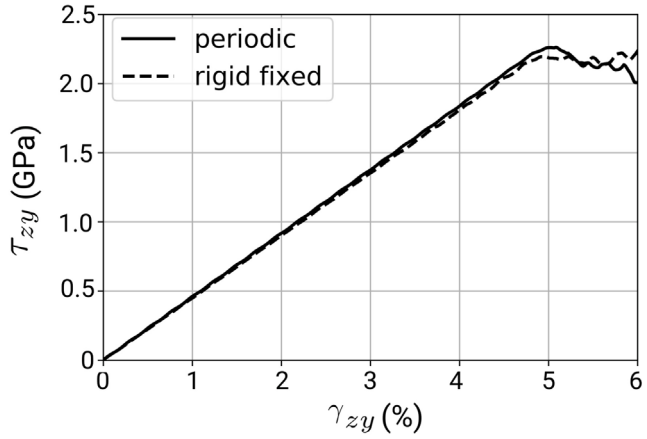

Fig. E.11. Shear stress–strain curve for an exterior Frank partial dislocation under simple shear: solid and dash lines for periodic and rigid fixed boundary conditions in dislocation emission direction (X direction). After the Frank partial dislocation dissociation ($\gamma_{zy} \approx 4.8\,\%$), the further transmission & reflection reactions occur at an almost constant shear stress (dash lines in range $\gamma_{zy} \sim 4.85\%$ to 5.73% corresponding to Supplementary Movie 1 (Fig. F.12)). Only a slight decrease in shear stress (solid line) with further increasing strain is observed due to periodic boundary conditions.

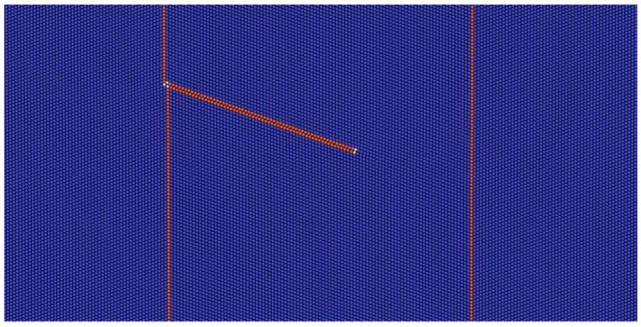

Fig. F.12. Supplementary Movie 1 (first frame) with symmetric simple shear ($\gamma_{zy} \sim 4.85\%$ or $\tau_{zy} \sim 2.22\,\text{GPa}$) and rigid fixed boundary conditions in dislocation emission direction (X–axis). Lattice dislocation emission and further three cycles of repeatable transmission & reflections are observed ($\gamma_{zy} \sim 4.85\%$ to 5.73% in Fig. E.11).

Appendix E. Shear stress–strain curve

See Fig. E.11.

Appendix F. Supplementary movie

See Figs. F.12 and F.13.

Appendix G. Supplementary data

Supplementary material related to this article can be found online at https://doi.org/10.1016/j.msea.2026.150362.

Data availability

Data will be made available on request.

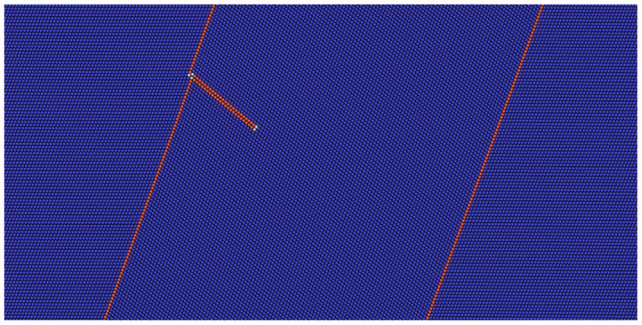

Fig. F.13. Supplementary Movie 2 (first frame) of preliminary test with non-symmetric simple shear ($\gamma_{zy} \sim 4.72\%$ or $\tau_{zy} \sim 2.14\,\text{GPa}$) with 20° clockwise rotated twin boundary and rigid fixed boundary conditions (X–axis). Lattice dislocation emission and further two cycles of repeatable transmission & reflections are observed ($\gamma_{zy} \sim 4.72\%$ to 5.34%).

References

[1] C. Koch, D. Morris, K. Lu, A. Inoue, Ductility of nanostructured materials, Mrs Bull. 24 (1999) 54–58.
[2] M.A. Meyers, A. Mishra, D.J. Benson, Mechanical properties of nanocrystalline materials, Prog. Mater. Sci. 51 (2006) 427–556.
[3] M. Dao, L. Lu, Y. Shen, S. Suresh, Strength, strain-rate sensitivity and ductility of copper with nanoscale twins, Acta Mater. 54 (2006) 5421–5432.
[4] Y. Shen, L. Lu, Q. Lu, Z. Jin, K. Lu, Tensile properties of copper with nano-scale twins, Scr. Mater. 52 (2005) 989–994.
[5] L. Lu, R. Schwaiger, Z. Shan, M. Dao, K. Lu, S. Suresh, Nano-sized twins induce high rate sensitivity of flow stress in pure copper, Acta Mater. 53 (2005) 2169–2179.
[6] K. Lu, L. Lu, S. Suresh, Strengthening materials by engineering coherent internal boundaries at the nanoscale, Science 324 (2009) 349–352.
[7] L. Lu, Y. Shen, X. Chen, L. Qian, K. Lu, Ultrahigh strength and high electrical conductivity in copper, Science 304 (2004) 422–426.
[8] L. Lu, X. Chen, X. Huang, K. Lu, Revealing the maximum strength in nanotwinned copper, Science 323 (2009) 607–610.
[9] X. Li, Y. Wei, L. Lu, K. Lu, H. Gao, Dislocation nucleation governed softening and maximum strength in nano-twinned metals, Nature 464 (2010) 877–880.
[10] J. Hirth, R. Pond, J. Lothe, Spacing defects and disconnections in grain boundaries, Acta Mater. 55 (2007) 5428–5437.
[11] V. Yamakov, D. Wolf, S.R. Phillpot, A.K. Mukherjee, H. Gleiter, Dislocation processes in the deformation of nanocrystalline aluminium by molecular-dynamics simulation, Nat. Mater. 1 (2002) 45–49.
[12] K. Lu, Stabilizing nanostructures in metals using grain and twin boundary architectures, Nat. Rev. Mater. 1 (2016) 1–13.
[13] J.R. Greer, It's all about imperfections, Nat. Mater. 12 (2013) 689–690.
[14] Y.M. Wang, F. Sansoz, T. LaGrange, R.T. Ott, J. Marian, T.W. Barbee, A.V. Hamza, Defective twin boundaries in nanotwinned metals, Nat. Mater. 12 (2013) 697–702.
[15] Y. Wang, B. Wu, M. Sui, Dynamical dislocation emission processes from twin boundaries, Appl. Phys. Lett. 93 (2008).
[16] L. Zhang, W. Mao, M. Liu, Y. Shibuta, Mechanical response and plastic deformation of coherent twin boundary with perfect and defective structures, Mech. Mater. 141 (2020) 103266.
[17] N. Lu, K. Du, L. Lu, H. Ye, Transition of dislocation nucleation induced by local stress concentration in nanotwinned copper, Nat. Commun. 6 (2015) 1–7.
[18] E. Marquis, D. Medlin, Structural duality of $1/3\langle 111\rangle$ twin-boundary disconnections, Phil. Mag. Lett. 85 (2005) 387–394.
[19] E. Ma, Y. Wang, Q. Lu, M. Sui, L. Lu, K. Lu, Strain hardening and large tensile elongation in ultrahigh-strength nano-twinned copper, Appl. Phys. Lett. 85 (2004) 4932–4934.
[20] M. Sennour, S. Lartigue-Korinek, Y. Champion, M. Hÿtch, HRTEM study of defects in twin boundaries of ultra-fine grained copper, Phil. Mag. 87 (2007) 1465–1486.
[21] X. Gao, L. Dai, Y. Zhao, Twin boundary-dislocation interactions in nanocrystalline Cu-30% Zn alloys prepared by high pressure torsion, J. Mater. Res. Technol. 9 (2020) 11958–11967.
[22] H. Gleiter, The formation of annealing twins, Acta Metall. 17 (1969) 1421–1428.
[23] J. Hirth, R. Balluffi, On grain boundary dislocations and ledges, Acta Metall. 21 (1973) 929–942.
[24] J. Li, G.M. Pharr, C. Kirchlechner, Quantitative insights into the dislocation source behavior of twin boundaries suggest a new dislocation source mechanism, J. Mater. Res. 36 (2021) 2037–2046.

[25] A.P. Thompson, H.M. Aktulga, R. Berger, D.S. Bolintineanu, W.M. Brown, P.S. Crozier, P.J. in 't Veld, A. Kohlmeyer, S.G. Moore, T.D. Nguyen, R. Shan, M.J. Stevens, J. Tranchida, C. Trott, S.J. Plimpton, LAMMPS - a flexible simulation tool for particle-based materials modeling at the atomic, meso, and continuum scales, Comp. Phys. Comm. 271 (2022) 108171, http://dx.doi.org/10.1016/j.cpc.2021.108171.
[26] Y. Mishin, M. Mehl, D. Papaconstantopoulos, A. Voter, J. Kress, Structural stability and lattice defects in copper: Ab initio, tight-binding, and embedded-atom calculations, Phys. Rev. B 63 (2001) 224106.
[27] P. Hirel, Atomsk: A tool for manipulating and converting atomic data files, Comput. Phys. Comm. 197 (2015) 212–219.
[28] P.M. Anderson, J.P. Hirth, J. Lothe, Theory of Dislocations, Cambridge University Press, 2017.
[29] A. Stukowski, Visualization and analysis of atomistic simulation data with OVITO-the Open Visualization Tool, Modelling Simul. Mater. Sci. Eng. 18 (2010) http://dx.doi.org/10.1088/0965-0393/18/1/015012.
[30] A. Stukowski, V.V. Bulatov, A. Arsenlis, Automated identification and indexing of dislocations in crystal interfaces, Modelling Simul. Mater. Sci. Eng. 20 (2012) 085007.
[31] E. Bitzek, P. Koskinen, F. Gähler, M. Moseler, P. Gumbsch, Structural relaxation made simple, Phys. Rev. Lett. 97 (2006) 170201.
[32] W. Cai, V.V. Bulatov, J. Chang, J. Li, S. Yip, Periodic image effects in dislocation modelling, Phil. Mag. 83 (2003) 539–567.
[33] S. Suresh, K. Dang, S.J. Fensin, Sensitivity of dislocation-GB interactions to simulation setups in atomistic models, Comput. Mater. Sci. 221 (2023) 112085.
[34] X. Zhou, Thermodynamic analysis of dissociation of periodic dislocation dipoles in isotropic crystals, RSC Adv. 10 (2020) 35062–35071.
[35] V. Bulatov, W. Cai, Computer Simulations of Dislocations, vol. 3, OUP Oxford, 2006.
[36] Z. Jin, S. Dunham, H. Gleiter, H. Hahn, P. Gumbsch, A universal scaling of planar fault energy barriers in face-centered cubic metals, Scr. Mater. 64 (2011) 605–608.
[37] P. Branicio, J. Zhang, D. Srolovitz, Effect of strain on the stacking fault energy of copper: a first-principles study, Phys. Rev. B—Condensed Matter Mater. Phys. 88 (2013) 064104.
[38] P. Müllner, P.J. Ferreira, On the energy of terminated stacking faults, Phil. Mag. Lett. 73 (1996) 289–298.
[39] Z.-H. Jin, P. Gumbsch, E. Ma, K. Albe, K. Lu, H. Hahn, H. Gleiter, The interaction mechanism of screw dislocations with coherent twin boundaries in different face-centred cubic metals, Scr. Mater. 54 (2006) 1163–1168.
[40] Z.-H. Jin, P. Gumbsch, K. Albe, E. Ma, K. Lu, H. Gleiter, H. Hahn, Interactions between non-screw lattice dislocations and coherent twin boundaries in face-centered cubic metals, Acta Mater. 56 (2008) 1126–1135.
[41] Q. Fang, F. Sansoz, Influence of intrinsic kink-like defects on screw dislocation–coherent twin boundary interactions in copper, Acta Mater. 123 (2017) 383–393.
[42] T. Zhu, H. Gao, Plastic deformation mechanism in nanotwinned metals: An insight from molecular dynamics and mechanistic modeling, Scr. Mater. 66 (2012) 843–848.
[43] J. Wang, N. Li, O. Anderoglu, X. Zhang, A. Misra, J. Huang, J. Hirth, Detwinning mechanisms for growth twins in face-centered cubic metals, Acta Mater. 58 (2010) 2262–2270.
[44] V. Yamakov, D. Wolf, S. Phillpot, A. Mukherjee, H. Gleiter, Deformation-mechanism map for nanocrystalline metals by molecular-dynamics simulation, Nat. Mater. 3 (2004) 43–47.
[45] N.Q. Vo, R.S. Averback, P. Bellon, A. Caro, Yield strength in nanocrystalline Cu during high strain rate deformation, Scr. Mater. 61 (2009) 76–79.
[46] H. Idrissi, K. Renard, L. Ryelandt, D. Schryvers, P. Jacques, On the mechanism of twin formation in Fe–Mn–C TWIP steels, Acta Mater. 58 (2010) 2464–2476.
[47] N. Lu, K. Du, L. Lu, H. Ye, Motion of 1/3⟨111⟩ dislocations on Σ3 {112} twin boundaries in nanotwinned copper, J. Appl. Phys. 115 (2014).
[48] Y. Zhu, X. Wu, X. Liao, J. Narayan, L. Kecskés, S. Mathaudhu, Dislocation–twin interactions in nanocrystalline fcc metals, Acta Mater. 59 (2011) 812–821.
[49] Y. Zhu, J. Narayan, J. Hirth, S. Mahajan, X. Wu, X. Liao, Formation of single and multiple deformation twins in nanocrystalline fcc metals, Acta Mater. 57 (2009) 3763–3770.
[50] M. Sennour, S. Lartigue-Korinek, Y. Champion, M.J. Hÿtch, Local strain analysis in twin boundaries in ultrafine grained copper, J. Mater. Sci. 43 (2008) 3806–3811.
[51] S. Poulat, B. Décamps, L. Priester, Weak-beam transmission electron microscopy study of dislocation accommodation processes in nickel Σ=3 grain boundaries, Phil. Mag. A 77 (1998) 1381–1397.
[52] L. Li, N.M. Ghoniem, Twin-size effects on the deformation of nanotwinned copper, Phys. Rev. B—Condensed Matter Mater. Phys. 79 (2009) 075444.
[53] T. Ezaz, M.D. Sangid, H. Sehitoglu, Energy barriers associated with slip–twin interactions, Phil. Mag. 91 (2011) 1464–1488.
[54] Z. Wu, Y. Zhang, D. Srolovitz, Dislocation–twin interaction mechanisms for ultrahigh strength and ductility in nanotwinned metals, Acta Mater. 57 (2009) 4508–4518.
[55] Z. Shen, R. Wagoner, W. Clark, Dislocation and grain boundary interactions in metals, Acta Metall. 36 (1988) 3231–3242.
[56] S.-W. Kim, J.H. Kim, In-situ observations of deformation twins and crack propagation in a CoCrFeNiMn high-entropy alloy, Mater. Sci. Eng.: A 718 (2018) 321–325.
[57] J. Kacher, I. Robertson, Quasi-four-dimensional analysis of dislocation interactions with grain boundaries in 304 stainless steel, Acta Mater. 60 (2012) 6657–6672.
[58] Y. Liang, X. Yang, K. Ming, S. Xiang, Q. Liu, In situ observation of transmission and reflection of dislocations at twin boundary in CoCrNi alloys, Sci. China Technol. Sci. 64 (2021) 407–413.
[59] M. Dupraz, S.I. Rao, H. Van Swygenhoven, Large scale 3-dimensional atomistic simulations of screw dislocations interacting with coherent twin boundaries in Al, Cu and Ni under uniaxial and multiaxial loading conditions, Acta Mater. 174 (2019) 16–28.
[60] J. Zhang, H. Zhang, H. Ye, Y. Zheng, Twin boundaries merely as intrinsically kinematic barriers for screw dislocation motion in FCC metals, Sci. Rep. 6 (2016) 22893.
[61] T. Zhu, J. Li, A. Samanta, H.G. Kim, S. Suresh, Interfacial plasticity governs strain rate sensitivity and ductility in nanostructured metals, Proc. Natl. Acad. Sci. 104 (2007) 3031–3036.
[62] S.I. Rao, M. Dupraz, C. Woodward, T. Parthasarathy, Response surface for screw dislocation: Twin boundary interactions in FCC metals, Acta Mater. 195 (2020) 681–689.
[63] M. Chassagne, M. Legros, D. Rodney, Atomic-scale simulation of screw dislocation/coherent twin boundary interaction in Al, Au, Cu and Ni, Acta Mater. 59 (2011) 1456–1463.
[64] N. Li, J. Wang, A. Misra, X. Zhang, J. Huang, J. Hirth, Twinning dislocation multiplication at a coherent twin boundary, Acta Mater. 59 (2011) 5989–5996.
[65] C. Hong, N. Tao, X. Huang, K. Lu, Nucleation and thickening of shear bands in nano-scale twin/matrix lamellae of a Cu–Al alloy processed by dynamic plastic deformation, Acta Mater. 58 (2010) 3103–3116.
[66] Z. Kou, R. Huang, Y. Yang, T. Feng, S. Tang, S. Lan, L. Yang, Revealing the atomic-scale evolution of sessile disconnections on twin boundaries during deformation, Scr. Mater. 221 (2022) 114956.
[67] D. Barnett, J. Lothe, An image force theorem for dislocations in anisotropic bicrystals, J. Phys. F: Met. Phys. 4 (1974) 1618.